

JOSHUA

The Journal of Science and Health at the University of Alabama



2015

Volume 12

About the Cover:

M20, commonly known as the Trifid Nebula is an emission and reflection nebula composed primarily of hydrogen gas. It can be found within the constellation Sagittarius and is roughly between 2200 and 7600 light-years from Earth. This picture was taken using the Etsorn Observatory at New Mexico Institute of Mining and Technology

David Wang, the photographer, is an undergraduate majoring in Astronomy at California Institute of Technology. He was born and raised in Oregon where he would often drive hours to go stargazing.

2014-2015 JOSHUA Staff

Executive Editor:

Paula Adams

Editorial Director:

Grant Fairchild

Editors:

Amanda Volk

Caitlin Thomas

Faculty Sponsor:

Dr. Guy Caldwell

All rights to the articles presented in this journal are retained by the authors. Permission must be granted for replication by any means of any of the material.

Disclaimer: The views of the authors do not necessarily reflect those of the staff of JOSHUA or The University of Alabama.

Questions should be directed to joshua.alabama@gmail.com, and more information and all archived volumes are available at bama.ua.edu/~JOSHUA.

Table of Contents

The P-Squared Method of Orbital Determination	
James Parkes	4
Laboratory-Scale Automated Polymer Solar Cell Fabrication via Slot Die Coating	
Nick Johnson	11
Electrical Properties of Metal/Ferroelectric/Metal Thin Film Capacitors	
Gregory Cabot	15
Surface Modification of Nanostructured Iron Oxide Electrodes for Alternative Energy	
Christian Palmer	21
Fluorescence-Intermittence of Single CdSe@ZnS Semiconductor Quantum Dots on Ag Nanowire Substrate	
Michael Rogers.....	25
Metabolic Flux Model to Optimize <i>n</i>-butanol Production by <i>Clostridium tyrobutyricum</i>	
Sarah McFann.....	29
High Productivity, Serum-free, Suspension CHO Cell Culture Process Development for Anticancer Therapeutic Protein	
Joanna Urli.....	35
Digitizing the Algal Herbarium at The University of Alabama (UNA)	
Joseph Cardosi.....	39
Ecological Determinants of Blood Glucose in the Diamondback Water Snake <i>Nerodia rhombifer</i>	
Danny Laderberg.....	43
Microbial Effect on Age-Related Neurodegenerative Disorders	
Anthony James.....	51

The P-Squared Method of Orbital Determination

James Parkes¹, Manjul Pahwa²

Faculty Mentor: Michael Faison³

¹Department of Physics, The University of Alabama, Tuscaloosa, Alabama 35487

²Columbia University, New York, New York, 10027

³Yale University, New Haven, Connecticut 06520

Many of the methods used to determine the orbits of objects, such as asteroids, produce erroneous results at various points throughout their actual orbital path. These errors occur because many methods, such as Gauss's Method of orbital determination, rely on angles to calculate the asteroid's orbit, and it can be shown that these methods fail when that angle is a multiple of $\pi/2$. However, astronomers cannot always wait for asteroids to reach more favorable locations. Thus, they need access to an alternative method.

By taking advantage of a phenomenon known as parallax, it is possible to create a method for honing in on the actual orbit of the asteroid. Parallax enables one to determine the position of the asteroid relative to Earth at a single point in time. By combining this information with data gathered over two more observation sessions, it is possible to create a list of orbits. Finally, by comparing the predicted orbital data with the actual observed locations, it is possible to determine which is the asteroid's actual orbit.

Introduction

Every day thousands of objects known as asteroids travel around the sun alongside the planets. Most of these are bound to orbits that lie between Jupiter and Mars. However, a few of these early Solar System remnants pass relatively close to Earth, Asteroid 1627 Ivar being a prime example of this. These asteroids, known as Near-Earth asteroids, have the potential to either wreak unimaginable devastation on society or to supply humanity with large quantities of raw materials. In either case, the ability to accurately determine an asteroid's orbit is crucial. Although a variety of orbital determination methods (ODMs) exist, many of these break down at various points throughout the asteroid's orbit. One example is Gauss's Method of orbital determination (GM) which breaks when the Sun, Earth, and asteroid (SEA) form angles that are approximately integer multiples of $\pi/2$ due to taking the sine and cosine of this angle.

However, sometimes researchers are only able to gather data when the asteroid is in one of these locations. Thus, researchers need to have access to alternative methods of orbital determination. One possible way to achieve this goal is to make an ODM that does not depend on the SEA angle. One can remove this dependence by utilizing a phenomenon known as parallax to calculate the distance between the asteroid and Earth. Through Newtonian mechanics it can be shown that the orbit of an asteroid can be calculated

simply by knowing the position and velocity of the asteroid at a single point in time [1]. This means that if one were able to create a position vector based on the asteroid's apparent position in the sky and its distance determined by parallax, then all one must do is calculate the asteroid's velocity vector.

This vector can be computed by using the asteroid's apparent location at two other times. By implementing the apparent change in position of the asteroid between the first and second observations, it is possible to generate multiple guesses as to what the velocity vector might be. Each of these will generate a prediction as to where the asteroid should be at the time of the final observation. By comparing the predicted locations to the actual one, it is actually possible through repeated analysis to hone in on the asteroid's real velocity vector. The end result of this process is that the asteroid's orbit may be calculated.

Calculating Parallax

When one looks at the background sky, most objects, such as stars, appear to be stationary relative to one another. However, when an object, like an asteroid, passes close to the Earth it may appear to be at multiple locations when viewed at the same time from various places on Earth's surface. This can be seen in figure 1. Note that for background objects the shift is so small that it can be assumed to be negligible.



Figure 1: A representation of the parallax of a nearby object relative to the distant stars

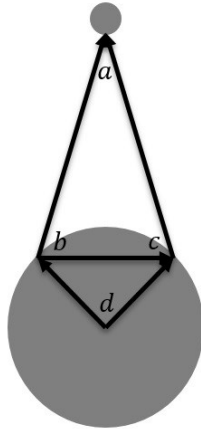


Figure 2: A schematic imaginary vectors in order to help determine the distance of an object based on parallax

Figure 1 demonstrates the parallax of an asteroid as seen from two different locations on Earth. The figure demonstrates how the asteroid can appear to be at two different positions, with respect to the background stars, depending on the observer's location.

Using the properties of vectors, it is possible to find the distance between the asteroid and Earth from this parallax shift. Figure 2 will act as a visual to help calculate this parallax.

First, one must draw vectors from c to $a(\vec{\rho}_c)$ and from b to $(\vec{\rho}_b)$. The angle between these is referred to as the parallax angle (angle a). At this point only the directions of the vectors, their unit vectors, can be found.

The unit vector in the direction of any object in the sky is given by the following equation, where a is its right ascension, δ is its declination, and $\hat{\rho}$ is its unit vector [1]:

$$\hat{\rho} = \begin{bmatrix} \cos \alpha \cdot \cos \delta \\ \sin \alpha \cdot \cos \delta \\ \sin \delta \end{bmatrix} \quad (1)$$

Note that in this paper a single column matrix will be used to represent a vector. By implementing equation (1), the unit vectors for both $\vec{\rho}_b$ and $\vec{\rho}_c$ can be found. To do this, let a_b and δ_b and $\hat{\rho}_b$ and a_c and δ_c and $\hat{\rho}_c$ represent the right ascensions, declinations, and unit vectors of $\vec{\rho}_b$ and $\vec{\rho}_c$ respectively.

Thus:

$$\hat{\rho}_b = \begin{bmatrix} \cos \alpha_b \cdot \cos \delta_b \\ \sin \alpha_b \cdot \cos \delta_b \\ \sin \delta_b \end{bmatrix} \quad (2)$$

And:

$$\hat{\rho}_c = \begin{bmatrix} \cos \alpha_c \cdot \cos \delta_c \\ \sin \alpha_c \cdot \cos \delta_c \\ \sin \delta_c \end{bmatrix} \quad (3)$$

Vectors are not bound to a particular point in space. Thus, the angle between two vectors should be equal to the angle between their unit vectors. This means that one should be able to determine the parallax angle (a) by utilizing the dot product of the unit vectors represented in equations (2) and (3). This gives:

$$\cos(a) = \hat{\rho}_b \cdot \hat{\rho}_c$$

$$a = \arccos(\hat{\rho}_b \cdot \hat{\rho}_c) \quad (4)$$

Now, vector \vec{bc} from figure 2 must be calculated. This can be done by applying vector subtraction on the two vectors traveling from the center of the Earth to the two observation sites on the surface of the Earth. Figure 2 represents these as \vec{db} and \vec{dc} . Finding these vectors requires three variables to be known about both locations: the radius of the Earth (which for simplicity's sake in this paper will be assumed to be constant throughout the globe), the latitude, and the local sidereal time which we will define as r_e , u , and t respectively. From these variables the vector from the center of the Earth to any location on the Earth's surface (\vec{e}) can be calculated as:

$$\vec{e} = r_e \cdot \begin{bmatrix} \cos t \cdot \cos u \\ \sin t \cdot \cos u \\ \sin u \end{bmatrix} \quad (5)$$

Using equation (5), it is possible to determine values for \vec{db} and \vec{dc} . Subtracting \vec{db} from \vec{dc} produces:

$$\vec{d} = \vec{dc} - \vec{db} \quad (6)$$

where \vec{d} is the vector from point b to point c in figure 2. Looking at the magnitude of this vector, it can be seen that the length of one side of $\triangle ABC$ and the angle opposite are both known. This suggests that the Law of Sines can be implemented to find the length of the other two sides. However, first one of the other two angles of the triangle must be calculated. $\angle CBA$, which will be referred to as b , can be found by taking the dot product of $\hat{\rho}_b$ and \vec{d} . This yields:

$$\begin{aligned} \hat{\rho}_b \cdot \vec{d} &= |\vec{d}| \cos b \\ b &= \arccos\left(\frac{\hat{\rho}_b \cdot \vec{d}}{|\vec{d}|}\right) \quad (7) \end{aligned}$$

Now, all the information necessary to find ρ_c (the magnitude of $\vec{\rho}_c$) is known. This calculation can be done by utilizing the results of equations (2), (4), and (7) along with the Law of Sines. Carrying out this computation produces:

$$\begin{aligned} \frac{d}{\sin a} &= \frac{\rho_c}{\sin b} \\ \frac{d}{\sin(\arccos(\hat{\rho}_b \cdot \hat{\rho}_c))} &= \frac{\rho_c}{\sin\left(\arccos\left(\frac{\hat{\rho}_b \cdot \vec{d}}{|\vec{d}|}\right)\right)} \\ \rho_c &= \frac{d \cdot \sin\left(\arccos\left(\frac{\hat{\rho}_b \cdot \vec{d}}{|\vec{d}|}\right)\right)}{\sin(\arccos(\hat{\rho}_b \cdot \hat{\rho}_c))} \quad (8) \end{aligned}$$

This equation gives the position of the asteroid relative to the Earth at a single point in time. Combining this with the known unit vector in the direction of $\vec{\rho}_c$ gives:

$$\vec{\rho} = \vec{\rho}_c = \rho_c \cdot \hat{\rho}_c$$

Angular Displacement

Once the distance to the asteroid (ρ_c) has been found, the angular displacement relative to a second observation session can be easily calculated.

Figure 3 depicts an asteroid at two different times as viewed from the same location on Earth. However,

this is only a simplistic model. In reality Earth both moves relative to the Sun and rotates slightly even over these small time intervals. In order to accurately determine an asteroid's orbit, these small changes in position must be compensated for.

Figure 4 readily demonstrates that not taking into account the motion of the Earth may significantly impact the value of the angle a . Compensating for this change in position, however, is relatively simple because the Earth's orbit and rotation have been accurately documented.



Figure 3: A simplified model of an asteroid moving relative to the Earth.

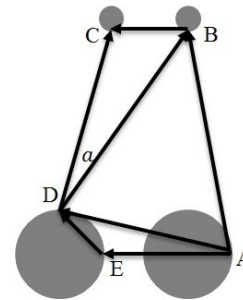


Figure 4: A representation of the asteroid's motion relative to Earth's orbital and rotational motion.

By analyzing the Earth's position at the time of parallax and at the time of the second observation, a displacement vector describing the change in the Earth's position between the two observation sessions can be created. Because vectors are not bound by spatial coordinate, this vector can be shifted to the point on Earth's surface where the parallax distance was calculated from. This is represented by point A in Figure 4. Note that now the other end of the vector falls on the surface of the Earth at the time of the second observation. This is depicted by vector \vec{AE} in Figure 4.

However, the rotation of the Earth must still be accounted for. By utilizing the rotation rate of the Earth and time elapsed between the two observations, a rotational displacement vector can be generated. In Figure 4 this is represented as \vec{ED} .

Thus, the net change in position of the observation site can be calculated as $\vec{AE} + \vec{ED} = \vec{AD}$. Now, the vector $\vec{\rho}$ must be shifted to the location of observation at the second observation time. Note that in figure 4, $\vec{\rho} = \vec{AB}$. This means that the vector $\vec{\rho}_b$ which runs from point D to point B is:

$$\vec{\rho}_b = \vec{\rho} - \vec{AD} \quad (10)$$

In order to compute the angle a , a vector in the direction of \vec{DC} must be found. The unit vector \widehat{DC} can be computed by equation (1). By knowing the values of $\vec{\rho}_b$ and \widehat{DC} , it can be shown through an application of the vector dot product that:

$$a = \arccos\left(\frac{\widehat{DC} \cdot \widehat{\rho}_b}{|\widehat{DC}|}\right) \quad (11)$$

Thus, the angular displacement of the asteroid over the course of the two observation sessions is a .

Orbital Velocity

In order to determine the orbit of an asteroid, both the asteroid's position and velocity relative to the Sun must be known at a single point in time. If the velocity vector relative to the Earth at the time of the initial observation can be calculated, then the position and velocity relative to the Sun can be found.

Unfortunately, it is often difficult to compute motion in the $\widehat{\rho}_b$ direction because the observer is only able to see motion perpendicular to $\vec{\rho}_b$. This is depicted in figure 5. However, it turns out that the actual displacement can be found through an iterative estimation method that uses data from a third observation session.

To do this, a value for the velocity of the asteroid, \vec{v} , must be calculated assuming that the asteroid's displacement vector is perpendicular to $\vec{\rho}_b$. To do this, we must first find vector \vec{BC} as seen in the second of the two diagrams. This can be done through vector

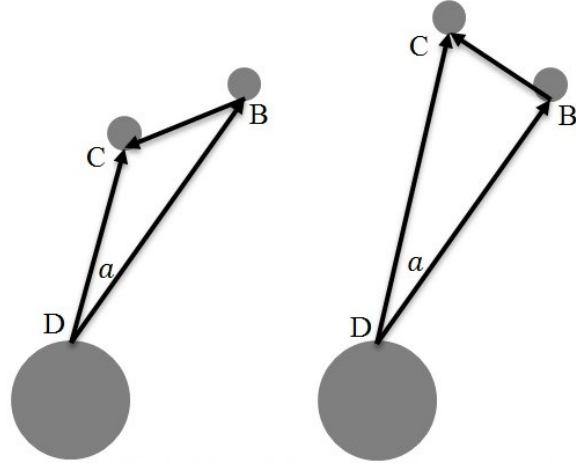


Figure 5: The first diagram shows how the Earth and the Asteroid appear in reality with respect to one another as seen by an outside observer. The second reveals the fact that the observer on Earth cannot see the radial component of the motion because all the observer can distinguish is the angular change in position of the asteroid.

subtraction. However, the magnitude of the vector \vec{DC} which will now be referred to as ρ_c , is still unknown. Because of the assumption about the asteroid's displacement, ΔBCD is a right triangle. Thus, by utilizing trigonometry it can be shown that:

$$\begin{aligned} \cos a &= \frac{\rho_b}{\rho_c} \\ \rho_c &= \frac{\rho_b}{\cos a} \end{aligned} \quad (12)$$

Thus, it follows that:

$$\vec{\rho}_c = \rho_c \cdot \widehat{DC} \quad (13)$$

By combining equations (10) and (13), the displacement vector from point B to point C can be found to be:

$$\vec{\rho}_\tau = \vec{\rho}_c - \vec{\rho}_b \quad (14)$$

Note that ρ_τ is in the direction of the velocity vector; however, it is a displacement vector, not a velocity vector. Now, let the time elapsed between the two observations be represented by $\Delta t = t_2 - t_1$ ¹.

$$\frac{\Delta \vec{\rho}}{\Delta t} = \frac{\vec{\rho}_\tau}{t_2 - t_1}$$

¹ t_1 and t_2 represent the times of the first and second observations respectively

Because the changes in time and position between the two observations are small relative to the entire orbit, these can be approximated as differential steps. It follows that:

$$\begin{aligned} \vec{v} &= \frac{d\vec{\rho}}{dt} \approx \frac{\Delta\vec{\rho}}{\Delta t} \\ &= \frac{\vec{\rho}_\tau}{t_2 - t_1} \quad (15) \end{aligned}$$

Finding the Orbit

Now, using the position of the Earth at the time of the second observation, the asteroid's position and velocity vectors relative to the Sun can easily be calculated. As depicted in figure 6, the vector \vec{SD} represents the vector from the Sun to the observer. Using this vector and vector addition, the position vector from the Sun to the asteroid at the time of the first observation can be shown to be:

$$\vec{r}_b = \vec{\rho}_b + \vec{SD} \quad (16)$$

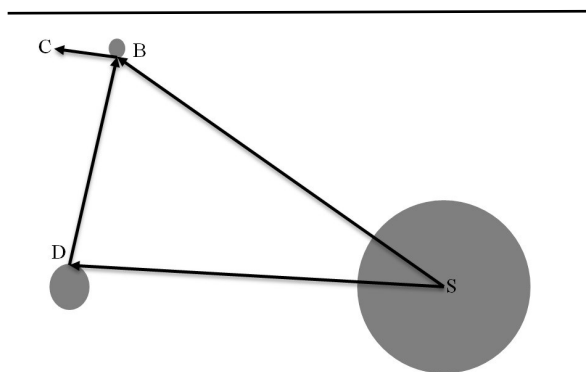


Figure 6 (above): The diagram depicts the Sun, Earth, and asteroid as well as all of the position vectors in order to allow the asteroid's position and velocity relative to the Sun to be calculated.

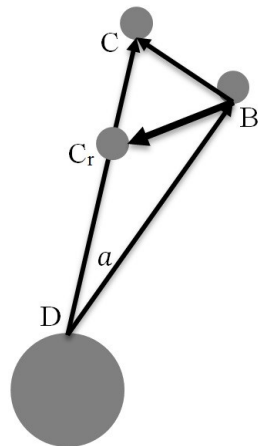


Figure 7 (left): The diagram depicts an overlay of the two diagrams in figure 5

Because vectors are independent of coordinate system, the velocity vector calculated in equation (15) is also the velocity vector relative to the Sun.

However, this velocity vector was found by assuming that the asteroid's velocity has no component in the $\hat{\rho}_b$ direction. In reality this is extremely unlikely. As can be seen in figure 7, \vec{v} as calculated earlier actually points along \vec{BC} rather than \vec{BC}_r . Thus, through the use of trigonometry, the actual velocity vector can be found to be:

$$\vec{v}_r = \left(\frac{k}{v} \cdot \tan(a) + 1 \right) \vec{v} + k \cdot \hat{\rho}_c \quad (17)$$

Where \vec{v}_r is the asteroid's real velocity vector and k is a scalar multiplier.

This means that if the value of k can be computed, then the actual velocity will be known. Unfortunately, this value cannot be directly calculated. Thus, an iterative method must be used to estimate k . To start this process, it must be assumed that $k = 0$. As a result, both \vec{r}_b and \vec{v} are known. By applying Newton's Laws of Motion and Gravity to these vectors, the orbital elements of the asteroid can be determined. From these orbital elements, an ephemeris can be generated which will enable the right ascension and declination of the asteroid to be calculated at any point in time [2].

Utilizing this ephemeris, the theoretical right ascension of the asteroid at the time of a third observation can be found. However, because it is unlikely that $k = 0$, the actual right ascension is likely to be different. Taking the difference between the actual value and the theoretical value gives:

$$\alpha_{net} = \alpha_{actual} - \alpha_{guess} \quad (18)$$

Unfortunately, equation (18) alone is not enough to give any information about k . In order to determine the sign of k , first a small value of k such as $k = \pm \frac{|v|}{10}$ should be chosen. By plugging these values into equation (17) and generating a new ephemeris for both cases, the right ascensions predicted for the third observation by the guessed values of k can be found.

These will be referred to as a_{+guess} and a_{-guess} respectively. Calculating their net right ascensions yields:

$$\begin{aligned}\alpha_{+net} &= \alpha_{actual} - \alpha_{+guess} \\ &\text{and} \\ \alpha_{-net} &= \alpha_{actual} - \alpha_{-guess} \quad (19)\end{aligned}$$

To determine which sign of k produces a velocity vector closer to the actual velocity vector these net values must be compared to the net value for $k = 0$ calculated in equation (18). This gives:

$$\begin{aligned}\alpha_{+diff} &= \alpha_{net} - \alpha_{+net} \\ &\text{and} \\ \alpha_{-diff} &= \alpha_{net} - \alpha_{-net} \quad (20)\end{aligned}$$

The correct sign of k will produce the equation where the sign of the difference is the same sign as a_{net} . This is because a_{net} should be farther from the actual value than a guess in the correct direction but closer than a guess in the wrong direction.²

While the sign of k is important, the actual scalar value is still unknown. In order to find k , an iterative method must be used. To carry out these calculation, an initial value of k must be chosen. Rather than just choosing an arbitrary value that may or may not in fact be larger than the actual value, which is necessary for the guessing method to succeed, the escape velocity of the asteroid offers a prime choice for a starting value for k . This is because in order for the asteroid to be in a stable orbit around the Sun, its velocity must be less than the escape velocity. Thus:

$$|k_{initial}| = v_{escape} = \sqrt{\frac{2GM_{sun}}{r}} \quad (21)$$

Now, all of the components necessary to begin the iteration process have been found. Note that the sign of $k_{initial}$ must be the same as that determined by equation (20). The net right ascension of this value of k must be found as demonstrated earlier. The second value of k to be guessed will be:

$$k = k_{prev} - \frac{k_{prev}}{2} \quad (22)$$

²If both signs should prove to be the same, then a smaller initial value for k should be chosen.

If the sign of a_{diff} (the difference between the net right ascension of the previous guess and the net right ascension of the current guess) is the same as the sign of the net right ascension calculated from k_{prev} , then $k_{prev} = k$ and this step must be repeated. However, if the sign of the a_{diff} changes, then k_{prev} must be redefined as $k_{prev} = k$ after which k itself must be redefined as:

$$k = k_{prev} + \frac{k_{prev}}{2} \quad (22)$$

This process must be repeated by changing the sign of the second term every time the sign of a_{diff} changes until the net right ascension equals zero. Once this has been achieved, the actual value of \vec{v}_r can be calculated by equation (18). Thus, both the position vector and the velocity vector of the asteroid are known. From these, the asteroid's real orbital elements can be found.

Discussion

Many methods for determining the orbit of an object around the Sun exist. However, these often possess limitations. Researchers need access to as many methods as possible because their research cannot always wait for the data to conform to the method.

The orbital determination method developed in this paper offers researchers a method that is independent of the asteroid's angular position with respect to the Earth and Sun. Through the use of parallax and apparent motion, the P-Squared Method allows researchers to calculate both the object's position and velocity, which give the object's orbital elements.

However, just like any method of orbit determination, the P-Squared Method has its own limitations. The most significant of these lies in the fact that in order to calculate parallax, images of the object at the same point in time from two different locations on the Earth are required.

Acknowledgements

We would like to thank Dr. Michael Faison for all of his help and encouragement over the course of the development of the P-squared Method.

We would also like to acknowledge all of our fellow team members--Matthew Zhu, Dahlia Baker, Aparna Narendrula, and Jackie Liu--from the Summer Science Program who worked with us attempting to determine the orbit of 1627 Ivar using the Method of Gauss at a point where the method breaks down.

Furthermore, we would like to thank our parents for always encouraging us to strive to do our best.

References

[1] Faison MD. (2011). Angles-Only Orbit Determination from Three Observations: Method of Gauss. Summer Science Program.

[2] Faison MD. (2010). Step-by-Step Guide to Generating an Ephemeris. Summer Science Program.

About the Author

Originally from Spanish Fort, Alabama, James Parkes is currently a Sophomore majoring in Electrical Engineering and Physics at the University of Alabama. He is also a member of the Computer-Based Honors Program. He is currently conducting research with Dr. Jerome Busenitz in the Department of Physics and Astronomy and with Dr. Dawn Williams in the Department of Physics and Astronomy. In addition to his love for education and research, James Parkes is an active member in campus politics where he hopes to help make campus better for all students. After graduating he intends to pursue a graduate degree in physics

Laboratory-Scale Automated Polymer Solar Cell Fabrication via Slot Die Coating

Nick Johnson, Vahid Badali, Ali Cortez, Matthew Gawlik, Christina Gimenez, Gunnar Pierce, Joseph Wolfe, Sheng Bi, Michael Ikegami, Shoieb Shaik, and Dr. Dawen Li*

Faculty Mentor: Dawen Li – dawenl@eng.ua.edu

Department of Electrical and Computer Engineering, The University of Alabama, Tuscaloosa, AL 35487

Polymer-based organic solar cells in conjunction with flexible substrates provide the possibility of automated mass-produced solar cells. While the efficiency of organic solar cells has not yet reached the efficiency of the most advanced traditional solar cells, improved polymer blends with advanced production schemes could yield the economies of scale necessary for ubiquitous solar energy. We provide a proof of concept of a slot die based printer that deposited both PEDOT hole transport and active layers with integrated annealing capability for solar cell production. We were able to obtain a power-conversion efficiency of 0.5% for a bulk heterojunction solar cell consisting of phenyl-C-butyric acid methyl ester (PCBM) and poly(3-hexylthiophene) (P3HT) as sunlight absorber.

Index Terms—Organic Polymer Solar Cells, Slot Die Coating, Flexible Substrate

Introduction

Organic polymer solar cells have seen a lot of research due to their ability to be processed using solutions. The majority of polymer-based organic solar cells fabricated in labs are created via spin coating. This process is successful on a small scale to investigate novel polymer blends and device engineering for achieving higher power-conversion efficiencies (PCE). Currently, the highest PCE in polymer-based organic solar cells has reached ~11%. The spin-coating process does not directly correlate to large-scale fabrication via roll-to-roll printing on flexible substrates. To achieve appropriate market share as a valid product, organic solar cells must be produced on a large-scale in order to account for their low power-conversion efficiency [1].

In this paper we provide a proof of concept for a roll coater that correlates more directly to large-scale fabrication of polymer-based organic solar cells. Our setup requires no vacuum and can deposit both hole transport and active layers with integrated thermal annealing capability.

Our paper analyzes the success of our roll coater in synthesizing polymer bulk heterojunction (BHJ) solar cells using P3HT:PCBM as active sunlight absorbing materials. P3HT:PCBM material system fabricated via traditional laboratory methods has PCEs in the range of 3-5% and via slot die methods similar to ours have demonstrated PCEs up to 1.6%.

[2,3,4,5]. We chose this material system because it has been thoroughly studied, so there are many different specifications available with which to judge the quality of our solar cell devices, including but not limited to the surface roughness, thickness of layers, and of course the PCE of our solar cells [1,2,6,7].

Roll Coater Characteristics

The roll coater is comprised of three functional components. The drumhead supports the flexible substrate and is rotated. A heater internally concentric to the drumhead heats the drumhead, allowing the integrated annealing process. Finally, a slot die head in connection with a syringe pump “prints” the polymer layers onto the flexible substrate.

Drumhead

An aluminum cylinder with a 3 inch outer diameter and 2.5 inch inner diameter was used as the drumhead seen in Figure 1. The flexible substrate was attached to the drumhead. The length of the drumhead was approximately four inches, and 1 inch of printable width was used for device fabrication. A gear motor was used to rotate the drumhead and substrate for printing. The drumhead rotating speeds range from tangential speeds of 1 m/min to 4 m/min.

Heater

A 250-Watt band heater was set stationary and concentrically within the drumhead to provide the heating required for thermal annealing with the con-

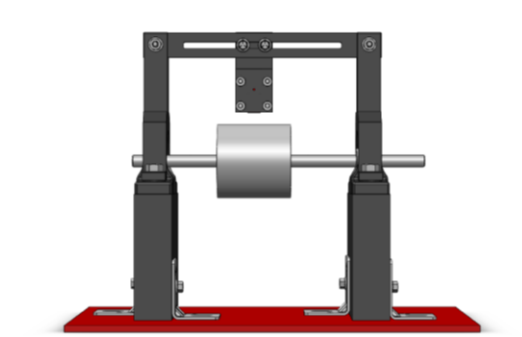


Figure 1. Schematic of roll coater prototype

figuration shown in Figure 2. Since both the drumhead and band heater were cylindrical, the heat provided was uniform. A proportional-integral-derivative (PID) controller with feedback provided by a thermocouple was used to set the temperature of the heater.

Slot Die Head in Connection with Syringe Pump

A variety of continuous roll-to-roll compatible deposition methods have been studied for solar cell fabrications [3,8,9,10,11]. We chose to go with slot die coating because it proved to be the simplest implementation. Due to the success in literature, we used a simple geometry for our slot-die head [3,8,9,10,11]. In order to control the flow rate through the slot die head, we used a syringe pump (NE-300 Syringe Pump). This allowed us to use standard connections such as a 1.0 μm filter, a Luer lock, and 2mm outer diameter Teflon tubing in order to interface between the programmable syringe pump and the slot die head.

Solar Cell Fabrication

Our fabrication process included the deposition of two separate layers and incorporated two separate annealing processes. Below we detail what our inputs were as well as our method for depositing and annealing them in sequence.

Materials

Our substrate was an Indium Tin Oxide (ITO) coated Polyethylene Terephthalate (PET) flexible foil purchased from Sigma-Aldrich. The thickness of the substrate was 5 mm with a resistivity of 60 ohms per square meter. Strips of the substrate were cut to the size of 8 inches by 0.5 inches. P3HT was purchased from Rieke Metals as Poly (3-hexylthiophene-2,5-diyl), regioregular, Electronic grade, and PCBM was purchased from Nano-C as C 71-butyric acid methyl ester [70]PCBM (99+% purity). The solvent used was chlorobenzene purchased

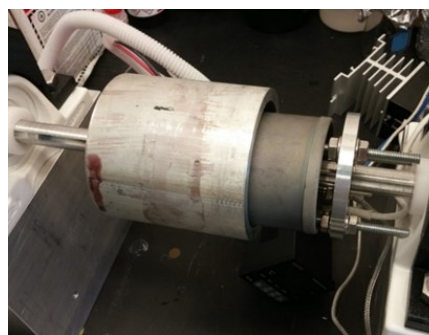


Figure 2. Heater concentrically in drumhead

from VWR as Chlorobenzene (99%). The P3HT:PCBM (1:1 weight ratio) at a concentration of 20 mg/ml was used in solar cell fabrication. PEDOT was purchased from Heraeus as Clevis P VP AI 4083.

Slot Die Coating

First, the substrate was attached to the drumhead and aligned with the slot die head. A tangential rotational speed of 1.5 m/min was used throughout. Then the PEDOT layer was deposited onto the substrate with a flow rate through the slot-die head of 0.75 mL/min. A temperature of 70° C was established on the drumhead. The layer was then annealed for 20 minutes. A temperature of 90° C was then established on the drumhead. The P3HT:PCBM solution was then deposited onto the PEDOT layer with a flow rate of 0.75mL/min through the slot die head. The P3HT layer was annealed for 5 minutes. Finally, the strip was cut into squares and, placed under a shadow mask, and the device fabrication was completed by thermal evaporation of an 80 nm Al cathode at rate of 2 $\text{\AA}/\text{s}$ in a vacuum of $5 \cdot 10^{-6}$ torr.

Characterization and Electrical Measurement

Atomic force microscopy (AFM) was used to evaluate the quality of the films produced via slot die coating. Current-voltage characterization of the printed solar cells was conducted using Agilent Technologies B1500A Semiconductor Device Analyzer under the illumination of AM1.5G, 100 mW/cm².

Results

After the successful setup of a small roll coater prototype, PEDOT and an active layer were deposited on PET flexible substrate for organic solar cell fabrication. Figure 3 (a) and (b) show the AFM images of surface morphology of the PEDOT layer only and P3HT:PCBM active layer on PEDOT, respectively. The roughness of PEDOT layer from slot

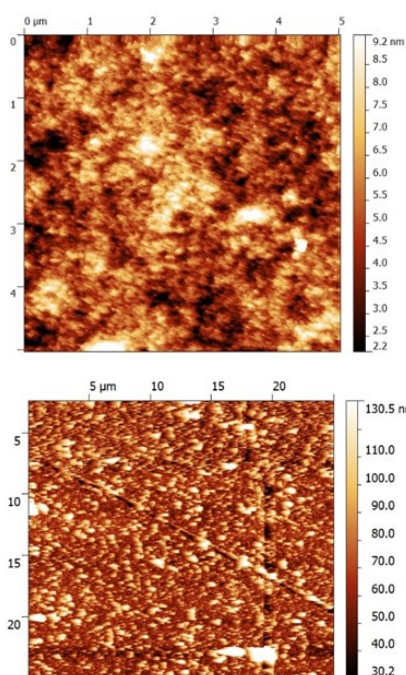


Figure 3. AFM image (5 μm X 5 μm) for the morphology of (a) PEDOT and (b) P3HT:PCBM active layer on PEDOT, respectively.

die coating is about 1.1 nm, which is comparable with that from traditional spin-coating, while the roughness of P3HT:PCBM active layer on top of PEDOT layer is about 17.7 nm, a little bit rougher than that from spin-coating.

In addition to the characterization of film surface roughness, a current-voltage (I-V) measurement was performed to calculate the power-conversion efficiency. Figure 4 represents the structure of organic solar cells. From the I-V curves shown in Figure 5, the maximum efficiency for our slot-die coated solar cells was PCE = 0.5%, which is lower but relatively on par with values for P3HT:PCBM based organic solar cells produced via similar methods [1,3,11].

The reduced PCE of the solar cells created with our roll coaters could result from the high thickness of our PEDOT layer, which is approximately 260 nm. The optimized thickness from spin-coating is about 90nm. The high thickness causes more charge carrier recombination, reducing the efficiency. The PEDOT thickness can be reduced by diluting the PEDOT solution and rotating the drumhead at higher speed. These schemes will be able to minimize PEDOT thickness while retaining film uniformity in deposition.

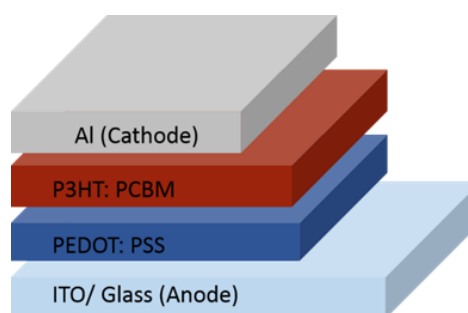


Figure 4. Schematic of organic solar cell

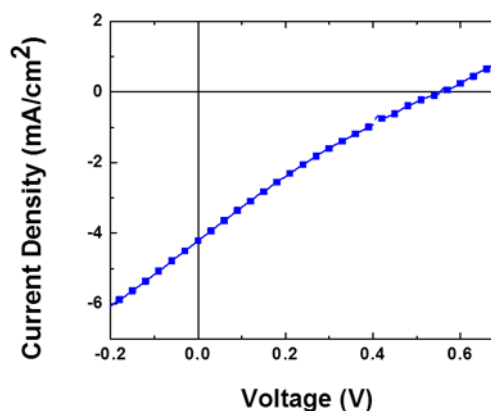


Figure 5. I-V curve of printed solar cells (inset) from roll coater on flexible substrate.

On the other hand, the efficiency could be further improved by operating the prototype in a nitrogen filled glove box instead of in ambient conditions. Due to the reactive nature of the organic materials, exposure to oxygen and moisture could be reducing the performance of our solar cells. Making solar cells using a roll coater in a glove box also allows for the opportunity to study the effect of humidity on performance of roll-coated solar cells.

Conclusion

In this study, we demonstrated working organic solar cells on flexible substrate using homemade roll coater. This slot-die coater has integrated heater for thermal annealing after deposition. This prototype is also small enough in scale that it should be able to easily fit inside a standard glove box so that it can be added into any lab with minimal inconvenience.

Using a well-studied P3HT:PCBM material system, our prototype's operation was confirmed. This success can be easily transferred to other polymers as well as multilayer structures with the slot die coater.

References

- [1] Deibel C & Dyakonov V.(2010). Polymerfullerene bulk heterojunction solar cells. *Rep. Prog. Phys.*, 73 (9):096401.
- [2] Blankenburg L, Schultheis K, Schache H, Sensfuss S & Schrodner M. (2009). Reel-to-reel wet coating as an efficient up-scaling technique for the production of bulk-heterojunction polymer solar cells. *Solar Energy Materials and Solar Cells*. 93:476-483
- [3] Dam HF & Krebs FC.(2012). Simple roll coater with variable coating and temperature control for printed polymer solar cells. *Solar Energy Materials and Solar Cells*, 97:191-196.
- [4] Sun Z, Xiao K, Keum JK, Yu X, Hong K, Browning J, Ivanov IN, Chen J, Alonzo J, Li D, Sumpter BG, Payzant EA, Rouleau CM, & Geoghegan DB. (2011). Ps-b-p3ht copolymers as p3ht/pcbm interfacial compatibilizers for high efficiency photovoltaics. *Advanced Materials*, 23(46):5529-5535.
- [5] Zimmermann B, Schleiermacher HF, Niggemann M & Wurfel U.(2010). Ito-free flexible inverted organic solar cell modules with high fill factor prepared by slot die coating. *Solar Energy Materials and Solar Cells*, 95:1587-1589.
- [6] Cai W, Gong X & Cao Y.(2010). Polymer solar cells: Recent development and possible routes for improvement in performance. *Solar Energy Materials and Solar Cells*, 94:114-127.
- [7] Yang X & Loos J.(2007). Toward high-performance polymer solar cells: the importance of morphology control. *Macromolecules*, 40(5):1353-1362.
- [8] Krebs FC.(2009). Fabrication and processing of polymer solar cells: A review of printing and coating techniques. *Solar Energy Materials and Solar Cells*, 93:394-412
- [9] Krebs FC.(2009). Polymer solar cell modules prepared using roll-to-roll methods: Knife-over-edge coating, slot-die coating and screen printing. *Solar Energy Materials and Solar Cells*, 93:465-475.
- [10] Krebs FC, Fyenbo J & Jorgensen M. (2010). Product integration of compact roll-to-roll processed polymer solar cell modules: methods and manufacture using flexographic printing, slot-die coating and rotary screen printing. *J. Mater. Chem.*, 20:8994-9001.
- [11] Sondergaard R, Hosel M, Angmo D, Larsen-Olsen TT & Krebs FC.(2012) Roll-to-roll fabrication of polymer solar cells. *Materials Today*, 15:36-49.

Acknowledgements

We would like to acknowledge the support for this capstone design project from the Scholarship Office and the Department of Electrical and Computer Engineering at The University of Alabama. This project was partially supported by NSF Grant # ECCS-1151140.

About the Authors

Nick, Vahid, Ali, Matthew, Christina, and Joseph are all Seniors in Electrical Engineering. Nick, Vahid, Ali, Christina, and Joseph graduated May of 2015. This was a yearlong Senior Design Project to fulfill the requirements for their respective majors in Electrical and Computer Engineering. Sheng Bi and Shoieb Shaik are graduate students who work in Dr. Li's lab. Michael Ikegami is a Junior in Electrical Engineering who also works in Dr. Li's lab. Dr. Li supervised this capstone design project.

Nick will be working for Lockheed Martin Space Systems, Christina will be working for Enercon Services, Gunnar will be working for Nucor Steel, Ali will be working for Jacobs Engineering Group, and Joe will be finishing his MBA through the STEM path to MBA at the University of Alabama.

Electrical Properties of Metal/Ferroelectric/Metal Thin Film Capacitors

Gregory Cabot, Vaishali Batra, Sushma Kotru

Faculty Mentor: Sushma Kotru

Department of Electrical Engineering, The University of Alabama, Tuscaloosa, AL, 35487

Metal/Ferroelectric/Metal (MFM) thin film capacitors were prepared using chemical solution deposition and sputtering. PLZT, a ferroelectric material commonly used for optical devices, and more recently for ferroelectric photovoltaic applications, was chosen for the purposes of this study. Pt, Au, and Al with different work functions were used as top metal electrodes. The effects of work function of top metal electrodes on the electric properties of these capacitor structures were investigated by measuring the Capacitance-voltage and Polarization-voltage. The results show that capacitance, spontaneous and remnant polarization of the MFM structures increase as the work function of the top metal electrodes increases. Pt as top metal electrode is observed to perform better in these capacitor devices.

Introduction

Lead Zirconium Titanate, $\text{Pb}(\text{Zr}_x\text{T}_{1-x})\text{O}_3$ is one of the most widely studied material system for a wide variety of applications. The interest in this system persists due to the ferroelectric, pyroelectric, and piezoelectric properties, making it a material of choice for nonvolatile random access memory (NVRAM), high power dielectric energy storage, high-performance ferroelectric capacitors, infrared sensors, and micro-electromechanical (MEMS) applications [1-3].

Lead Zirconium Titanate abbreviated as, PZT, is a solid solution of Lead Zirconate (PbZrO_3) and Lead Titanate (PbTiO_3). Above the Curie temperature, PZT is in the paraelectric phase exhibiting a cubic perovskite structure. The Curie point depends on Zr/Ti ratio and varies between $230^\circ\text{C} - 490^\circ\text{C}$. At temperatures below the Curie point, the PZT unit cell is distorted giving rise to a tetragonal phase (for high Ti concentrations, $\text{Zr/Ti} = 48/52$) or rhombohedral phase (for high Zr concentrations, $\text{Zr/Ti} = 52/48$). The distortion in the unit cell results in a dipole which is the source of spontaneous polarization in ferroelectric materials. A unit cell of PZT material with two polarization states (up and down) is shown in Figure 1(a) and (b). A shift in the center ions of $\text{Zr}^{4+}/\text{Ti}^{4+}$ with respect to the oxygen tetrahedron correspondingly leads to an up polarization state and a down polarization state. An electric field, when applied to the up polarization state of the crystal, can shift the $\text{Zr}^{4+}/\text{Ti}^{4+}$ ions and the oxygen tetrahedron in the opposite direction, causing polarization switching. This property is utilized for memory applications.

The tetragonal and rhombohedral ferroelectric phases are separated by a morphotropic phase boundary (MPB) at $x=0.48$ [4]. Thus at MPB, an abrupt structural change occurs with the variation of composition which is independent of temperature. In bulk ceramics significant enhancement in some physical properties are seen at the MPB composition [5]. However, this is not always true in the case of thin films as film orientation, microstructure, stress and other factors play an important role in achieving various properties.

Doping PZT has shown to improve various properties. As an example, PZT doped with Nb is reported to increase the effective transverse piezoelectric coefficient $-e_{31,f}$ [7] as well as ferroelectric response [8] making it a highly suitable material for Piezo MEMS and infrared devices [2-3]. Similarly, doping PZT with an appropriate amount of La has been shown to enhance the optical properties of the material making it an attractive material for optical applications such as optical MEMS, optical modulators/transducers and smart sensors [8-12]. Recently, a combination of ferroelectric properties and the optical transparency in PLZT has been utilized to exploit the use of this material for non-conventional photovoltaic devices [13-15].

In this study, PZT films doped with 5 % Lanthanum and having a Zr/Ti ratio of 54/46 ($\text{Pb}_{0.95}\text{La}_{0.05}\text{Zr}_{.54}\text{Ti}_{0.46}\text{O}_3$) were chosen to prepare Metal/Ferroelectric/Metal (here after referred to as MFM) capacitor structures. This composition was chosen based on the past work carried out by our group. The ferroelectric metal interface is reported to change the electrical behavior of the ferroelectric

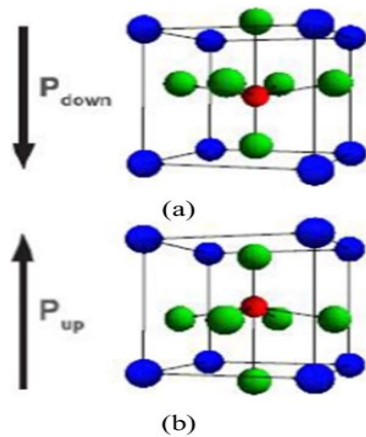


Figure 1: Unit cell structure of a PZT cubic perovskite structure with two polarization states (a) down (b) up [6].

films. This interface is important to realize the practicality of the films for memory devices or solar cells, as it is integral to the sensors performance to know the electrical behavior of films with the different electrodes [16]. Metal electrodes chosen for this study were Pt, Au and Al whose work functions are 5.3, 5.1 and 4.3 eV respectively. Variation of metal top electrodes allowed us to study the change in the electrical response of the capacitors to the work function of top electrodes.

Experimental Methods

The chemical solution deposition (CSD) method is a highly flexible method for fabrication of many materials, especially electronic oxide films. In this method, liquid precursor formulations are spun on the substrate and suitably heat treated to obtain crystalline formation. The CSD process steps include (i) preparation of suitable precursors, (ii) deposition/coating of precursor on the substrate to form thin film, (iii) pyrolysis, and (iv) annealing.

Preparation of the precursors using CSD method can be achieved via one of the three methods classified as (i) sol-gel: alkoxide precursors are used which undergo primarily hydrolysis and poly condensation (ii) metal-organic decomposition (MOD): carboxylate precursors are used which do not undergo significant condensation reactions and (iii) hybrid route: multiple precursor types are used which undergoes condensation reactions at several stages. Further details about this process can be obtained from the reference of Schwartz et al. [17]. Deposition of the precursor on the substrate can be achieved via (i) spin coating (ii) spray coating, and/or (iii) dip coating. In the following sections, we describe the methods used

for the preparation of the PLZT precursor and films for our work.

Preparation of PLZT Precursor

There are certain requirements which should be met to prepare a precursor using the CSD process. The most important requirements are that the precursor (i) should be soluble in the solvent to form a stable solution, (ii) should decompose or pyrolyze without leaving undesirable residues during the thermal process, (iii) elements except the cations must be released into gas phase during thermal treatment, (iv) components should not result in macroscopic phase separation during pyrolysis, (v) individual components should not crystallize during evaporation, (vi) should maintain homogeneity at atomic level, (vii) should have an acceptable wetting of substrate, and (viii) should not result in compositional non-uniformities during pyrolysis or the crystallization process [17].

MOD was used to prepare the $Pb_{0.95}La_{0.05}Zr_{.54}Ti_{0.46}O_3$ precursor. The PLZT precursor was obtained by dissolving lead acetate trihydrate ($Pb[CH_3COO_2]_2 \cdot 3H_2O$), lanthanum acetate ($La[CH_3COO]_3$), zirconium propoxide (Zr

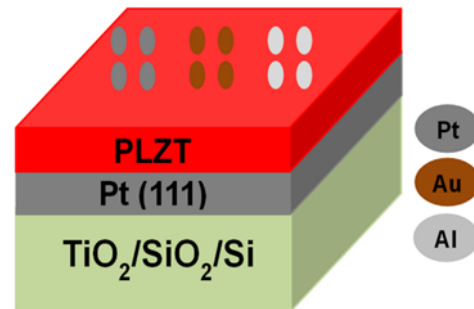


Figure 2: PLZT Capacitor Structure [19].

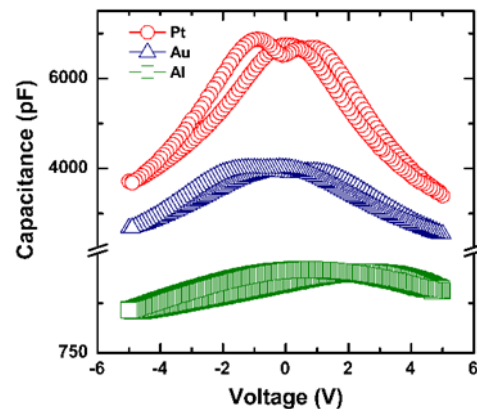


Figure 3: Capacitance as a function of voltage for three types of MFM capacitors.

[OCH₂CH₂CH₃]₄), and titanium butoxide (Ti [OCH₂CH₂CH₂CH₃]₄) in the solvent 2-methoxyethanol with intermittent heating and cooling. The concentration of the precursor solution was 0.4 M. More details about the process can be found from our previous publication [18].

Preparation of PLZT Films

PLZT thin films were deposited on Pt (111)/TiO₂/SiO₂/Si (100) substrate. The substrates were bought from a commercial vendor. A spin coater was used to prepare the films. The precursor was spin coated on the substrate at room temperature with a spin speed of 3000 rpm for 30 sec. After each deposition, the film was hydrolyzed at 120 °C for 2 minutes and pyrolyzed at 400 °C for 2 minutes, using a hot plate. The pyrolysis process ensures the conversion of solid inorganic materials into gases by indirect heat.

This process was repeated three times to achieve a film thickness of 210 nm. After triple coating and heating cycles, the PLZT films were annealed at 750 °C in flowing oxygen gas (2000 sccm) using a rapid thermal annealing (RTA) furnace for 2 minutes. A profilometer (Dektak) was used to measure the film thickness. Further details about the deposition process can be obtained from our previous publication [18].

Fabrication of MFM Capacitors

The MFM capacitor structures were fabricated by sputtering various metal electrodes on top of PLZT films. The sputter deposition of metal electrodes was carried out using a sputtering unit from Denton Vacuum (DV-502A). The films were loaded in the chamber on a specially designed holder. The unit was pumped down using a roughing pump to a low vacuum of 10⁻³ Torr. After the crossover pressure was achieved, the diffusion pump was switched ON and the unit was left pumping down to achieve a vacuum of ~10⁻⁶ Torr. Once the required vacuum was obtained, the diffusion pump was switched OFF and Ar gas was introduced in the chamber to maintain a pressure of 60 mTorr. A power supply was used to provide sufficient energy to ionize the Ar gas. Ar⁺ impacts the target with high energies and transfers their momentum to the target material thereby disrupting the atomic surface causing target atoms, ions, and electrons to be ejected and deposited on the substrate. When the desired thickness of top electrodes (Pt and Au) was achieved, the current was set to zero amps, Ar gas flow was stopped, and the chamber was vented to bring it to atmospheric pressure. At this point the

samples were demounted from the holder and were ready for measurements. A cartoon of MFM structures is shown in Figure 2. Electrodes of various shapes/sizes such as oval were sputtered on the film using a shadow mask, with the area of electrodes being $9.8 \times 10^{-8} \text{ m}^2$. It is pertinent to point out that the bottom metal electrode in all three cases was Pt and only the top electrodes were changed.

Characterization of Films/MFM capacitors

Once the film preparation was completed, films were characterized for structural and electrical properties. A Rigaku X-ray Diffraction (XRD) was used to confirm the crystallinity of the films (results not included in this paper). The electrical characterization of the capacitors was carried out using a probe station connected to an HP 4284A Impedance Analyzer which was then serially connected to LabVIEW interfaced computer. The capacitance-voltage (C-V) measurements were done in a range of -5 to +5 V. The permittivity and dielectric loss were measured as a function of frequency. The Polarization-Voltage (P-V) hysteresis loops were measured at a frequency of 1 kHz using a Ferroelectric Tester RT 6000 A from Radiant Technologies.

Results and Discussion

Capacitance Voltage

C-V measurements allow to understand the response of the capacitor to changes in voltage applied across the capacitor. The capacitances of the three MFM structures were measured by sweeping the bias voltage from -5 to 0 to 5 V and back from 5 to 0 to -5 V while measuring the capacitance at each corresponding voltage point. Figure 3 shows the C-V characteristics for the MFM structures with Pt, Au and Al as top metal electrodes. Measurements with Al top electrodes are published in our previous paper and shown here for comparison [20]. All the curves show butterfly behavior, which is a typical characteristic of a ferroelectric material.

As can be seen from Figure 3, Pt/PLZT/metal capacitors were found to have the highest capacitance (6752 pF) whereas the Al/PLZT/metal capacitors exhibited the lowest capacitance (953 pF). Thus, when Al, an electrode with lower work function was used as top metal electrode, it reduced the capacitance of the device by ~7 times compared to the Pt based devices.

The highest capacitances from Pt/PLZT/

metal capacitors can be attributed to their smaller space charge region which limits the amount of free electrons available near the surface of the ferroelectric metal interface.

Capacitance Frequency

The capacitors were then used to study the variances in their permittivity and tangential loss. Each film was subjected to a 1 V bias under varying frequencies in the range of 1 kHz to 1MHz. Figure 4 shows the capacitance-frequency response and tangential loss of the three MFM structures measured in the frequency range of 10^3 - 10^6 Hz.

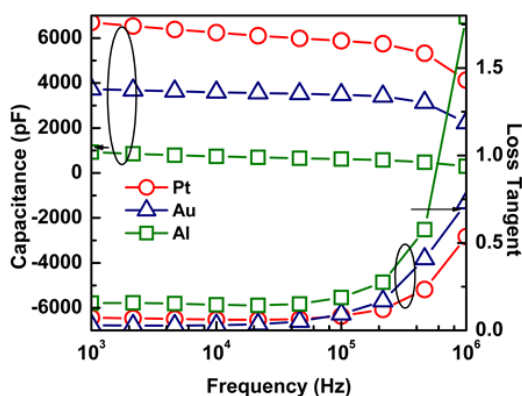


Figure 4: Frequency response of three types of MFM capacitors

From these measurements, it was found that Pt/PLZT/metal capacitors exhibited the highest capacitance of the three metals studied. Al/PLZT/Metal exhibits the lowest capacitance and the highest loss tangent of 0.16.

Ferroelectric Measurements

The polarization of the capacitor structures was measured as a function of applied voltage. The measurement was done using a bias of -20 V to 20 V, and normalized for the size of the electrode used. Figure 5 shows the P-V hysteresis loops with Pt, Au and Al as top electrodes.

The P-V loops indicate that all of the three MFM capacitors exhibit ferroelectric switching behavior, irrespective of top electrodes used. It can be observed that with Pt (or Au) as top electrodes, the capacitors show similar and symmetrical polarization loops. However, the hysteresis loop of the capacitor with Al electrode shows a lossy behavior suggesting the loss of ferroelectric properties.

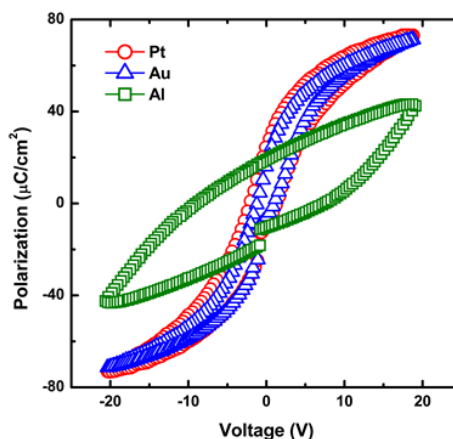


Figure 5: Polarization of the MFM Capacitors

The results obtained for capacitance, saturation polarization (P_s), remnant polarization (P_R), and dielectric loss for all the three capacitors along with the work function of each metal are summarized in Table 1. As is clear from this table, when the Pt top electrode is replaced by the Al electrode in the MFM capacitor structure, capacitance decreases from 6752 pF to 953 pF (~7.1 times) and P_s decreases from 72.79 to 42.47 $\mu\text{C}/\text{cm}^2$ (~1.7 times), permittivity decreases from 1745 to 240 (~7.3 times) and dielectric loss increases from 0.07 to 0.16 (~2.3 times).

Al has a strong tendency to form oxide layers at the ferroelectric metal interface, which could be the reason for a drop in all the measured electric parameters listed in Table 1.

The oxide layer formation is due to the relative ease that Al has of forming Al_2O_3 layers at the interfaces exposed to air for a long period of time. Even a brief exposure to oxygen can cause the formation of a 4-5 nm oxide layer on the surface, which then prohibits the formation of any more oxidation layers in the future. Al_2O_3 is an electric insulator,

Electrode	Work function (eV)	Capacitance (pF)	P_s $\mu\text{C}/\text{cm}^2$	P_R $\mu\text{C}/\text{cm}^2$	$\tan \delta$
Pt	5.3	6752	72.79	24.4	0.07
Au	5.1	3937	70.55	20.7	0.03
Al	4.28	953	42.47	19	0.16

Table 1 Capacitance, saturation polarization (P_s), permittivity and dielectric loss for the three capacitors with respect to work functions of top electrodes Pt, Au, and Al.

which causes the decrease of electrical properties seen in all the electric measurements. This oxide layer enhances the leaky current of the Al-based films, resulting in the curve shown in Figure 5, and decreasing the capacitance of the film. Thus the change in the shape of hysteresis loop seen in Figure 5 could be attributed to two reasons: lower work-function of Al top electrode [8] and a possible formation of a thin Al_2O_3 layer at the interface, owing to the tendency of Al to oxidize [20].

Conclusions

MFM capacitor structures, with PLZT as ferroelectric, and Pt, Au, and Al as top metal electrodes (having different work functions) were compared. The electrical properties of these devices were studied by measuring the capacitance, frequency response, dielectric loss, and polarization for different voltages. It was shown that the Al/PLZT/metal capacitors show a markedly decreased value for capacitance and polarization due to the formation of an oxidation layer at the interface of the electrode. Pt, on the contrary, showed a large improvement in electrical properties, in particular capacitance and polarization. Thus, it can be concluded that the choice of metal for the top electrode MFM capacitor has a large effect on the electrical performance. Metal of higher work function are seen to perform better in capacitor devices.

References

- [1] A. Datta, D. Mukherjee, S. Witanachchi, and P. Mukherjee (2014). Hierarchically Ordered Nano-Heterostructured PZT Thin Films with Enhanced Ferroelectric Properties. *Advanced Functional Materials*, 24-18: 2638–2647.
- [2] S. Wang, B. Ma, J. Deng, H. Qu, & J. Lou (2014). Fabrication and characterization of MEMS piezoelectric synthetic jet actuators with bulk-micromachined PZT thick film. *Microsystem Technologies*, 542:2278-2285.
- [3] A. Tommasi, G. Coletta, S.L. Marasso, M. Cocuzza, C.F. Pirri, D. Perrone, G. Canavese, S. Stassi, S. Bianco, D. Balma (2014). Process optimisation of a MEMS based PZT actuated microswitch. *Microelectronic Engineering*, 119: 137-140.
- [4] B. Jaffe, J. William, R. Cook, and H. Jaffe (1971). *Piezoelectric Ceramics*. Academic Press, 20-65.
- [5] F. Jona and G. Shirane (1962). *Ferroelectric Crystals*. McMillan.
- [6] G. Shirane, R. Pepinsky and B. Frazer (1956). *Acta Crystallographica*, 9:131.
- [7] J. Zhong, S. Kotru, H. Han, J. Jackson, and R. K. Pandey (2011). Effect of Nb Doping on Highly {100}-textured PZT Films Grown on CSD-prepared PbTiO₃ Seed Layers. *Integrated Ferroelectrics*, 130:1-11.
- [8] W. Wang, Q.X. Zhu, X.M. Li, M.M. Yang, X.D. Gao, X.Q. Zhao (2013). Effects of ferroelectric/metal interface on the electric properties of PMN-PT thin films epitaxially grown on Si substrates. *Journal of Materials Science: Materials in Electronics*, 24.10: 3782-3787.
- [9] K. Uchiyama, A. Kasamatsu, Y. Otani, and T. Shiosaki (2007). Electro-Optic Properties of Lanthanum-Modified Lead Zirconate Titanate Thin Films Epitaxially Grown by the Advanced Sol Gel Method. *Japanese Journal of Applied Physics*, 46:L244.
- [10] H. Shima, T. Iijima, H. Funakubo, T. Nakajima, H. Naganuma, and S. Okamura (2008). Electrooptic and Piezoelectric Properties of (Pb,La)(Zr,Ti)O₃ Films with Various Zr/Ti Ratios. *Japanese Journal of Applied Physics*, 47:7541-7544.
- [11] A. Zomorrodian, N. J. Wu, Y. Song, S. Stahl, A. Ignatiev, E. B. Trexler, and C. A. Garcia (2005). Micro Photo Detector Fabricated of Ferroelectric Metal Heterostructure. *Japanese Journal of Applied Physics*, 44:6105-6108.
- [12] K. Uchino and M. Aizawa (1985). Photostrictive Actuator Using PLZT Ceramics. *Japanese Journal of Applied Physics*, 24:139.
- [13] H.T. Huang (2010). Solar Energy Ferroelectric photovoltaics. *Nature Photonics*. 4:134-135.
- [14] M. Qin, K. Yao, and Y. C. Liang (2008). High efficient photovoltaics in nanoscaled ferroelectric thin films. *Applied Physics Letters*, 93:122904.
- [15] S. Y. Yang, J. Seidel, S. J. Byrnes, P. Shafer, C. H. Yang, M. D. Rossell, P. Yu, Y. H. Chu, J. F. Scott, J. W. Ager, L. W. Martin, and R. Ramesh. Above-bandgap voltages from ferroelectric photovoltaic devices. *Nature Nanotechnology*, 5:143-147.
- [16] Priya, S. Laxmi (2015). Transverse piezoelectric properties of {100} - Oriented PLZT[x/65/35] thin films. *Materials Chemistry & Physics*, 151: 308-311.
- [17] R. W. Schwartz (1997). Chemical Solution Deposition of Perovskite Thin Films. *Chemical Materials*, 9: 2325-2340.
- [18] V.N. Harshan, S. Kotru (2011). Effect of Annealing on Ferroelectric Properties of Lanthanum Modified Lead Zirconate Titanate Thin Films. *Integrated Ferroelectrics*, 130:73-83.
- [19] V. Batra, G. Cabot, V.N. Harshan, S. Kotru. Effect of work function of top electrodes on the electrical properties of PLZT thin film capacitors. *MINT Fall Review*; 2014; Tuscaloosa, AL.
- [20] H. V.N., and S. Kotru (2012). *Applied Physics Letters*, 100:17.

Acknowledgements

One of the authors (GC) would like to thank V. Batra and S. Kotru for their guidance and help during the course of study.

About the Author

Originally from Memphis, Tennessee, Gregory Cabot is a junior at the University of Alabama pursuing a degree in Electrical Engineering with a minor in Computer Based Honors. Gregory has been working with Dr. Kotru in the Department of Electrical Engineering for two years.

Surface Modification of Nanostructured Iron Oxide Electrodes for Alternative Energy

Christian R. Palmer, ZhiChao Shan, Shanlin Pan, Ph.D.

Faculty Mentor: Shanlin Pan

Department of Chemistry, The University of Alabama, Tuscaloosa, AL 35487

Hematite ($\alpha\text{-Fe}_2\text{O}_3$) has been extensively studied as a promising material for the water-splitting reaction in photoelectrochemical cells due to its capability of absorbing visible light and placement of its conduction bands suitable for water splitting. However, it has a poor interface for facilitating efficient water splitting and has a very short hole transfer length. To circumvent these problems and maximize photocurrent, other materials have been included to increase the hematite surface area and improve its interactions with water. Surface-coating with carbon-doped TiO_2 nanoparticles has shown promising results for the interface between hematite and water.

Introduction

An increasing global energy demand, along with rising awareness of increasing amounts of anthropogenic greenhouse gases in the atmosphere, has fueled a search for renewable and carbon-neutral energy sources [1]. The sun illuminates the earth with a very large amount of light every day, and the usage of less than one hundredth of that light energy has the potential to satisfy the entire planet's energy demands [2]. Moreover, harnessing solar energy represents what is truly the most sustainable energy source, as the sun is expected to last billions of years. Unfortunately, solar energy is periodic and inconsistent for a given location due to factors such as weather, whereas energy demand is not. Therefore, in order to wean the earth off of non-renewable energy sources, an efficient method must be developed to harvest and store solar energy. One of the more promising strategies to achieve this objective is the photoelectrochemical splitting of water, which stores energy from the sun in the bonds of elemental hydrogen and oxygen (Figure 1), as demonstrated by Fujishima and Honda in 1972; however, there is currently no known material that has been identified with the necessary stability, cost, and efficiency characteristics for usage in water splitting at a large scale [3].

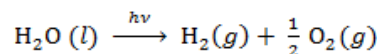


Figure 1: The splitting of water into its component elements due to light in the presence of a catalyst.

One promising candidate material for use in the water oxidation half reaction in photoelectrochemical water splitting is hematite ($\alpha\text{-Fe}_2\text{O}_3$), due to its decent absorption of visible light up to 590 nm, a very

positive valence band energy, and strong stability under water oxidation conditions [4]. Additionally, this material is abundant and non-toxic, giving it potential to be used safely in large-scale applications. Unfortunately, these positive characteristics are outweighed by low charge carrier mobility and short lifetimes, the combination of which results in a very short charge collection length and ultimately charge recombination. Simply put, hematite is not conductive enough to be used electrically. Historically, this has prevented its use as a material in solar water splitting. However, recent advances in nanostructuring the hematite and doping strategies have renewed interest in this material for use in photoelectrochemical water splitting [4, 5, 6].

One major issue in the way of efficient photoelectrochemical water oxidation with hematite electrodes is that an applied potential is required to produce a photocurrent. This onset potential is a product of two competing factors: surface state charge recombination due to lack of conductivity and slow water oxidation kinetics [7]. In order to overcome these obstacles, a variety of methods have been employed to modify the surface of hematite such that the required applied potential can be reduced. Titanium oxide modified with carbon (COT) is a very promising surface catalyst developed in the Pan group at the University of Alabama for the photoelectrochemical water splitting reaction. COT can be made in a thin film, plate form, or in powder form for catalyzing redox reactions because of its powerful conducting properties. As such, it is being studied currently, and a provisional patent was filed in 2014 [8]. In this work, it is believed that the conductive properties of COT may be able to increase the photocurrent density of hematite photoanodes by aiding in charge separation and

therefore reducing surface state recombination.

In this work, photoelectrochemical measurement techniques such as cyclic voltammetry were employed to investigate the effects of COT on the photocurrent-producing ability of hematite photoanodes. Thin-film hematite electrodes were prepared by a spin-coating method and were subsequently coated with the surface catalyst COT.

Methods and Materials

Fluorine-doped tin oxide (FTO)-coated glass substrates (Pilkington Glass, Energy Advantage™ Low-E) were cleaned successively via sonication (Omegasonics) in DI water, acetone (Fischer Scientific), DI water, isopropanol (Fischer Scientific), and DI water for 15 minutes in each step before being subjected to UV/Ozone for 15 minutes (Bioforce Nanosciences). A spin-coater (Chemat Technology) was then used to pre-treat the FTO substrates with a solution of Titanium (IV) isopropoxide in isopropanol (2% by volume) before spin-coating the substrates in aqueous 2.10 M $\text{Fe}(\text{NO}_3)_3 \cdot 9\text{H}_2\text{O}$ (ACROS Organics) solutions at 800 rpm for 9 seconds, followed by 3,000 rpm for 30 seconds. The glass substrates were then heat-dried on a hot plate (Fischer Scientific) at 80 °C before annealing in a cube furnace (Thermo Scientific) at 600 °C with a temperature climb rate of 50 °C per minute and a dwell time of 3 hours.

Samples coated in COT films were prepared by creating hematite electrodes, then by drop-coating the hematite surface with a suspension of COT powder in a dilute solution of Nafion in DI water. These drop-coated samples were subsequently placed in a vacuum oven (Isotemp, Model 282A) at 60 °C for 40 minutes to evaporate the solvent. Afterwards, the samples were placed in a tube furnace (Thermo Scientific) in an inert atmosphere of N_2 to anneal at 400 °C, with a climb rate of 50 °C per minute and a dwell time of one hour. The samples were left in the furnace until the temperature had dropped below 100 °C before removal.

The water oxidation properties of all hematite films, both coated and non-coated, were examined in contact with an aqueous 0.1 M NaOH (Fischer Scientific) electrolytic solution. Photoelectrochemical measurements were then made with a potentiostat (CH Instruments Electrochemical Analyzer, CHI1207A). A cyclic voltammetry technique was employed, sweeping from 0.4 V to 1.4 V and back to 0.4 V versus a silver wire quasi-reference (QRE) electrode.

Results

As previously mentioned, it is thought that coating the surface of hematite films with COT could improve photoelectrochemical water oxidation. It is hypothesized that this would be due to two factors. Firstly, the separated charges created by the absorption of light by hematite could be delocalized throughout the COT film due to its conductive properties. Secondly, a homogenous mixture of unusual Ti valence states could more easily facilitate the oxygen evolution reaction by allowing better adsorption of water onto its surface. It is hypothesized that the combination of these two factors could produce a superior electrode for photoelectrochemical water oxidation. In order to create a more accurate comparison, bare hematite electrodes were created and tested as the control before coating the electrodes with COT, which were then tested after the hematite surface was modified as well. This way, a before-and-after comparison could be made, removing the variability between batches as a potential factor affecting performance measurements of the electrodes. Figures 2 and 3 display the cyclic voltammetry measurement data collected before and after application of COT to hematite. These data were taken in two different scenarios for each sample. The data labeled as ‘dark’ were measured while the reaction setup was shielded from all light with a dark, opaque material in order to simulate dark conditions. The data labeled as ‘light’ were measured with a lamp illuminating the sample, in order to simulate the input of energy due to the sun. By measuring the current each sample in both light and dark conditions, the amount of additional current produced due to light shining on the sample can be determined.

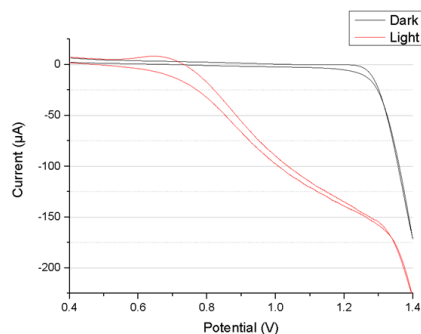


Figure 2 : Light (red) and dark (black) current of bare hematite electrode (vs. silver wire QRE) in 0.1 M NaOH solution.

It can be seen that modifying the surface of hematite films by layering a film of COT over the hematite most certainly affects the behavior of the

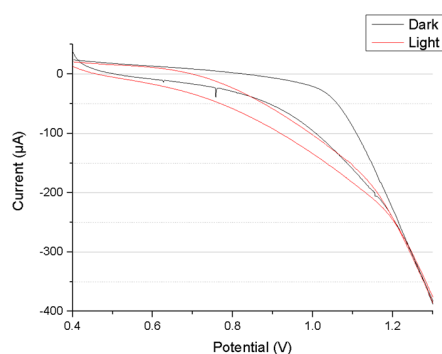


Figure 3: Light and dark current of COT-coated electrode (vs. silver wire QRE) in 0.1 M NaOH solution.

electrode. Unfortunately, the difference between the photocurrent and background (dark) current is less in COT-coated electrodes than it is in the bare hematite electrode, suggesting that less current is produced due to illumination of the electrode. This is likely due to the dark, opaque black color of the COT material. Since the thin hematite films are somewhat transparent, some of the light that is transmitted through the electrode reflects off of the back surface of the glass container used to conduct cyclic voltammetry testing and back onto the bare hematite electrode, thus causing it to be partially illuminated from the side opposite the light source as well. In the case of the COT-coated electrode, the opaque black color likely prevents this from happening. However, this minor setback is outweighed by the fact that the increase in background current causes an increase in total current produced in illuminated conditions. This is because COT is able to catalyze the oxidation of water even without assistance from conducting the separated charges produced in the light absorption in the hematite layer. As a result, the COT-coated electrode exhibits superior photoelectrochemical water oxidation characteristics above a potential of around 0.85 – 0.90 V vs. silver wire QRE where the total current is equal. Therefore, at volt biases above the equality point, the COT-coated electrode can produce the same total current as a bare hematite electrode with less applied potential, thus making the COT-coated electrode more energy efficient due to a favorable shift in photocurrent onset potential.

One important issue in utilizing the COT powder is that it does not readily attach to the hematite surface on its own. As a result, it comes off of the electrode easily, causing difficulty in testing the powder in contact with an aqueous electrolytic solution. If COT is ever to be utilized in large-scale applications, adjustments need to be made such that the COT coating is more durable. It is for this reason that the COT

electrodes were annealed in a tube furnace at 400 °C. Annealing the two materials at a high temperature creates a very tight interface between them and therefore increases durability significantly. This method, however, produces its own set of issues, because the oxygen in air would oxidize the COT at such temperatures, removing the carbon as it is oxidized into CO₂ and re-oxidizing the remaining Ti, thus leaving only a TiO₂ film on the hematite surface. It is for this reason that the COT-coated hematite electrodes were annealed in an inert atmosphere of nitrogen instead of air. Figure 4 exhibits the improvements made by this method.



Figure 4: COT-coated hematite photoelectrodes: one that was not annealed in N₂ (left), and one that was (right).

It should be noted that the plain COT coating was subjected to only one bout of cyclic voltammetric testing, while the annealed coating was subjected to ten. It is clearly visible that the annealed sample sustained minimal damage when compared to the non-annealed sample. Additionally, it should be noted that the water oxidation performance of the COT layer was not affected by the annealing process.

References

- [1] Moomow, W.; Yamba, F.; Kamimoto, M.; Maurice, L.; Nyober, J.; Urama, K.; Weir, T. 2011. In IPCC Special Report on Renewable Energy Sources and Climate change Mitigation. Cambridge University Press: United Kingdom and New York, NY, USA.
- [2] Lewis, N. S.; Nocera, D. G. 2006. Powering the planet: Chemical Challenges in solar energy utilization. *Proc. Natl. Acad. Sci. U.S.A.* **103**:15729.
- [3] Fujishima, A.; Honda, K. 1972. Electrochemical Photolysis of Water at a Semiconductor Electrode. *Nature.* **238**:37.
- [4] Lin, Y. J.; Zhou, S.; Sheehan, S. W.; Wang, D. W. 2011. Nanonet-Based Hematite Heteronanostructures for Efficient Solar Water Splitting. *J. Am. Chem. Soc.* **133**:2398.
- [5] Kay, A.; Cesar, I.; Gratzel, M. New Benchmark for Water Photooxidation by Nanostructured α -Fe₂O₃ Films. *J. Am. Chem. Soc.* **128**:15714.
- [6] Lin, Y.; Xu, Y.; Mayer, M. T.; Simpson, Z. I.; McMahon, G.; Zhou, S.; Wang, D. 2012. Growth of p-Type Hematite by Atomic Layer Deposition and Its Utilization for Improved Solar Water Splitting. *J. Am. Chem. Soc.* **134**:5508.
- [7] Cowan, A. J.; Barnett, C. J.; Pendlebury, S. R.; Barroso, M.; Sivula, K.; Grätzel, M.; Durrant, J. R.; Klug, D. R. 2011. Activation Energies for the Rate-Limiting Step in Water Photooxidation by Nanostructured α -Fe₂O₃ and TiO₂. *J. Am. Chem. Soc.* **133**:10134.
- [8] Shan, Z.; Pan, S.; Archana, P. S.; Gupta, A. Nano-COT Electrode: Nanostructured Ti-Based Anode Electrode Material for Enhanced Oxygen Evolution Reaction, Charge Storage and Solar Energy Conversion. United States Provisional Patent filed in 2014.

Acknowledgements

Special thanks go to the University of Alabama Chemistry REU Program for providing the opportunity to conduct the research in this work, as well as the National Science Foundation under Award Number CHE-1153120.

About the Author

Christian Palmer is a senior at the University of Alabama. He is originally from San Antonio, Texas and is currently completing a degree in Chemistry with a minor in Biology and a concentration in Biochemistry. In addition to his work in Professor Shanlin Pan's group in the Chemistry Department of the University, he is a member of the Balanced Man Scholarship Committee of the AL Beta Chapter of Sigma Phi Epsilon Fraternity, where he awards merit-based scholarships for rising freshman and sophomore men.

Fluorescence-Intermittence of Single CdSe@ZnS Semiconductor Quantum Dots on Ag Nanowire Substrate

Michael S. Rogers

Faculty Mentor: Shanlin Pan

Department of Chemistry, The University of Alabama, Tuscaloosa, AL 35487

Electrodeposition is used to grow silver nanowires (Ag NWs) onto an indium tin oxide (ITO) glass substrate. CdSe@ZnS core-shell semiconductor quantum dot (QD) samples are prepared on the Ag NW substrate using a drop-coating method for single QD imaging. Under a confocal microscope the illuminated sample is filmed with a high-speed camera. Using MATLAB software, fluorescent-intensity duration data is obtained for each single quantum particle identified in the film compilation image. The data shows that single particles usually have a brief fluorescent duration of only 1-2 frames of illumination. The results indicate that QDs are more likely to blink in short, quick intervals of time, as opposed to having long, drawn out periods of illumination.

Introduction

Research of inorganic semiconductor quantum dots (QDs) has been ongoing for several decades. Much of the excitement over QDs is because of their striking optical and electronic properties, such as multiple exciton generation (MEG), tunable band gaps via control over nanocrystal size and shape, large dipole moments, and large optical absorption coefficients. MEG happens when multiple electron-hole pairs are produced from the absorption of a single photon. These characteristics have the potential to increase the power conversion efficiency of QD-based solar cells beyond the Shockley-Queisser limit—the maximum theoretical efficiency of a solar cell—around 31% [1]. Given the potential of QDs in solar cell applications, it is no surprise that they are also potential inorganic replacements for organic absorbers in dye-sensitized solar cells (DSSC) [2,3,4]. QDs are utilized in a number of different instruments and applications including diodes, lasers, photonic devices, sensors, and as fluorescent labels for biomedical science [5].

Ag NWs are well known for an interesting surface plasmon effect which helps harvest incident light and enhance optical properties of semiconductor materials such as QDs, which exhibit fluorescent-intermittence, or “blink.” Other types of fluorophores, including single molecules, fluorescent proteins, polymer segments, and semiconductor nanowires would have interesting interactions with Ag NW as well. However, this research was specifically focused on the fluorescent characteristics of colloidal QDs are drop coated onto an Ag NWs substrate.

Semiconductor QDs usually have an average

diameter of 1-10 nm [3]. This results in band gap size dependence of the semiconductor particles, which in turn creates a blueshift in optical illumination of the particle as its size continues to decrease. By utilizing this unique characteristic, colloidal QDs (as chromophores) are able to alter and absorb, or even emit light anywhere in the visible spectrum and further beyond [2,4]. Another unique aspect of QDs is their blinking behavior. Both their blinking “on” and “off” times are fitted to a large power law that spans nine orders of magnitude in probability density and over five orders of magnitude in time. QDs are more likely to be fluorescent, or “on”, for very brief periods of time, as opposed to staying “on” for an extended period of time. This also means that QDs are “off” for longer periods in a prolonged dark state despite continuous laser excitation [6].

Experiment and Methods

To study the fluorescence-intermittent blinking behavior of single colloidal QDs on Ag NW substrates, a 0.17 mm thick ITO glass slide was used as the conductive substrate to grow Ag NWs and support QD particles. ITO glasses were thoroughly cleaned using the following solutions: sodium dodecyl benzene sulfonate (C₁₈H₂₉NaO₃S), ethanol (EtOH), deionized water, and isopropyl alcohol. First, the ITO glass slide was placed inside a secure glass container which was then filled with the first of the aforementioned solutions. The sample was then placed in a sonicator for about 10-15 minutes; afterwards, the glass container was flushed out using DI H₂O and the next cleaning agent was applied to the sample. This process was sequentially repeated for each additional solution. For the final step of the cleaning process, the ITO

glass was placed in a UV ozone machine for approximately 10-15 minutes. This measure helped create a clean surface for an even distribution of Ag NWs across the ITO substrate following electrodeposition. Ag nanowires were electrodeposited onto ITO electrode surface from a 250 ml aqueous solution of 0.1 mM silver nitrate. The completed Ag NW sample showed ideal characteristics for study with a smooth, even distribution of silver NWs that covered most of the ITO substrate. When held to the naked eye, the sample was clearly transparent with a low silver density.

Over the course of the research, many samples were made at various durations while maintaining the same dilution of 0.1 mM AgNO₃ for Ag NW growth. The duration of electrodeposition included 30 minute, and 1, 1.5, and 2 hour time frames. After several Ag NW samples were created, each sample was placed in a UV spectrometer to measure the absorbance of material. A clean, bare ITO glass slide was used as a control sample to aid in the comparison of several Ag NW samples of varying densities. As predicted, a longer electrodeposition time correlated linearly with a high density of Ag NWs in the sample, and thus a higher absorbance of light. For the study of fluorescence-intermittent single nanoparticles, a low absorbance from the Ag NW substrate is ideal because it allows for more light to be transmitted through the substrate to illuminate the quantum nanoparticles of interest. Therefore, a sample created using a smaller deposition time would absorb less light than a sample with a longer deposition. For this reason, the 30 minute deposition Ag NW sample was chosen for exhibiting a low absorbance—close to that of the bare ITO—and thus a high transmittance of light.

A commonly accepted idea for colloidal QDs, first proposed by Efros and Rosen, is that of a trapping state [6]. They stated that luminescence was quenched if a carrier, electron or hole is trapped in the surrounding matrix. In order to combat this “trap state”, colloidal QDs (CdSe) were over-coated with a higher band gap semiconductor (ZnS) to help prevent edge luminescence quenching of surface sites [2,7]. A specific dilution of 10 ng/mL CdSe@ZnS in Toluene was prepared; 10 mL of this solution was then drop-coated onto the Ag NW substrate. This dilution was used to increase the amount of data obtained for single particle QD and NW fluorescence, i.e., by limiting the dilution of 10 ng/mL QD in the solution, the maximum number of single particle quantum dots was able to be optically viewed through the microscope objective.

To reiterate, all QD fluorescence was studied using a confocal microscope while the sample underwent continuous laser excitation. CdSe has a band gap of 1.7 eV and can absorb light below 720 nm [3]. For QDs, as well as for the bare Ag NW substrate, fluorescence was observed using a 488 nm laser. The sample was optically viewed using a 100x magnification lens, and a 1.6x magnification microscope setting. A drop of immersion oil type-F, for fluorescence/ordinary microscopy, was placed on the upper face of the 100x magnification lens. The sample was then placed upright on the viewing objective. This allowed single particles in the sample to be readily and clearly viewed when illuminated by the 488 nm laser. All three samples were filmed while under continuous laser excitation using a high-speed camera and Andor software (with a resolution binning of 128x128 pixels) [7]. These films were then imported into MATLAB programming software for further study.

After importing the film to MATLAB, the fluorescence of each individual QD can be viewed from a single compilation image. This is made possible by condensing all the frames of the film into one; an example of such an image is seen in **Figure 1**. After the image is formed, MATLAB was able to determine the approximate locations of each point of light on the slide. While most individual points of light seen on the stock image are that of single particle QDs (fluorescing under continuous laser excitation), the larger “dots” are actually aggregated clusters of many single particle QDs [8]. The fluorescence of the Ag NW substrate itself can also be observed in the image background. However, in order to exclusively study the fluorescence-intermittence of single particles, MATLAB was used to differentiate between fluorescence data from the Ag NW substrate and aggregated clusters of QDs. For this reason, the program is able to differentiate between single quantum particles and aggregated clusters. This allows fluorescent trajectory data to be obtained for the single quantum particles

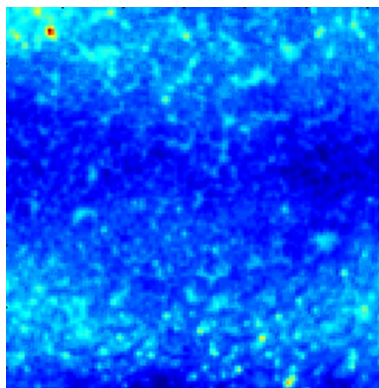


Figure 1. Colloidal CdSe@ZnS QDs fluorescing under continuous laser excitation.

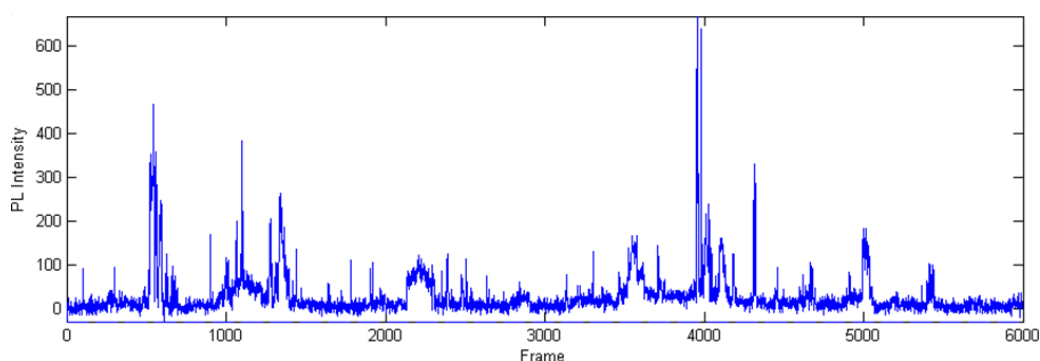


Figure 2. Fluorescence intensity trajectory of a single CdSe@ZnS QD.

observed. These trajectories must be manually altered to eliminate any substrate background fluorescence that interferes with the desired data.

When looking at a fluorescence trajectory plot for a single QD, the intensity appears to periodically peak, then return to a steady, lower background intensity. An example of such a plot is shown in **Figure 2**. The “background” intensity actually comes from the fluorescence of the substrate (Ag NW) itself; thus, it generally remains constant. The intensity fluctuations that are spiking, however, are those of a single QDs fluorescing. Taking a closer look at the intensity fluctuations, the intensity peaks are not equal; that is because typical fluorescence trajectories of single QDs do not mimic random telegraph noise. In other words, many intensities exist. Their fluorescence intensity is intermittent because the nanoparticles are exhibiting the characteristics instilled by quantum confinement of fluorophores [6]. Trajectories pertaining to aggregated clusters are removed from the analysis, so as to not skew the results from single particle QDs. After the particle trajectories are finalized, they are ready to be exported to Excel for data analysis.

Results and Discussion

Under continuous laser excitation the particles can be seen visibly blinking. The data obtained from the fluorescence-intensity trajectories quantifies the fluorescence-intermittent characteristics for single quantum nanoparticles. The fluorescent frequency and duration of each were in very close proximity to one another with only a few aggregated clusters visible. Specifically, the data shows the duration of all blinking “on” sequences

and how often the given durations occurred over the course of the film. This data is fitted to a power law, which can be seen in **Figure 3**. For single particles, the highest frequency of “on” states occur for only a few frames illumination; however, particles are also capable of experiencing prolonged periods of illumination as well as dark states. This phenomena is intriguing because of the unique electrical properties of QDs, i.e. multiple electron excitation. If the fluoresce capabilities of QDs could be fully understood, they could theoretically be utilized in new solar cells, increasing the maximum energy efficiency.

Conclusion

As a final point, it is apparent that semiconductor QDs exhibit power law distributions. While this phenomena is interesting, the result was an expected outcome given the characteristics of fluorophore substances. All fluorophores exhibit this intermittent blinking behavior when undergoing continuous laser excitation. This means that both quantum NW and Ag NW would mimic the same fluorescent characterizes as the single QD particles previously depicted. Therefore, the distribution seen in **Figure 3** will help gauge

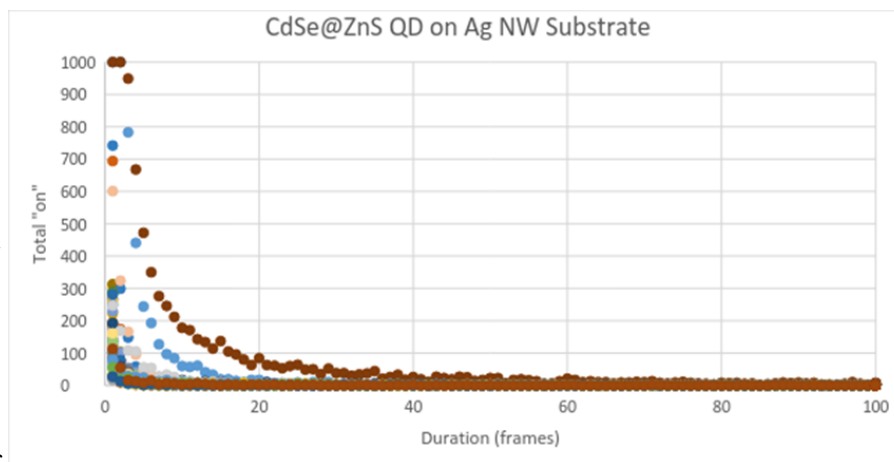


Figure 3. Frequency vs. duration of QD ON fluorescence states.

future experiments involving various fluorophore substances. The quality of the data obtained also lead me to believe that the Ag NW's, as a background substrate, have an ideal transparency for use in photoelectric studies. Future goals include the use of a bonding linker substance for QD attachment to Ag NW substrate, as well as examining different concentrations of CdSe@ZnS semiconductor particles.

References

- [1] Nozik AJ. (2002). Quantum dot solar cells. *Physica E*, 14:115-120.
- [2] Frantsuzov PA, Marcus RA. (2005). Explanation of quantum dot blinking without the long-lived trap hypothesis. *Physical Review B*, 72, 155321:1-10.
- [3] Rhee JH, Chun C, Diao EW. (2013). A perspective of mesoscopic solar cells based on metal chalcogenide quantum dots and organometal-halide perovskites. *NPG Asia Materials*, 68:1-17.
- [4] Shimizu KT, Woo WK, Fisher BR, Eisler HJ, Bawendi MG. (2002). Surface-Enhanced Emission from Single Semiconductor Nanocrystals. *Physics Review Letter*, 89, 117401:1-4.
- [5] Pilla V, Alves LP, Santana JF, Silva LG, Ruggiero R, Munin E. (2012). Fluorescence quantum efficiency of CdSe/ZnS quantum dots embedded in biofluids: pH dependence. *Journal of Applied Physics*, 112, 104704:1-5.
- [6] Frantsuzov PA, Kuno M, Janko B, Marcus RA. (2008). Universal emission intermittency in quantum dots, nanorods and nanowires. *Nature Physics*, 4:519-522.
- [7] Kuno M, Fromm DP, Hamann HF, Gallagher A, Nesbitt DJ. (2001). "On"/"off" fluorescence intermittency of single semiconductor quantum dots. *Journal of Chemical Physics*, 115:1028-1040.
- [8] Borys NJ, Lupton JM. (2011). Surface-Enhanced Light Emission from Single Hot Spots in Tollens Reaction Silver Nanoparticle Films: Linear versus Non-linear Optical Excitation. *Journal of Physical Chemistry*, 115:13645-13659.

Acknowledgements

I would like to first off thank the UA REU Program for providing an invaluable learning and research experience. I would like to thank the National Science Foundation, under award number CHE-1153120. I would like to thank Caleb Hill, and all of Dr. Pan's research group, for their continued guidance and support.

About the Author

Michael S. Rogers is a senior from Hoover, Alabama majoring in mechanical engineering at the University of Alabama. He first became involved with undergraduate research under the supervision of Dr. Bakker, where he designed (and 3D-printed) a flow cuvette vessel for use in a UV Spectrometer and worked on vacuum pumps. Later, he became affiliated with Dr. Pan through the REU Chemistry program at the University of Alabama where he continues research with semiconducting nanoparticles (QDs). In the future, he seeks employment in a progressive minded company that values the vast potential of renewable and sustainable energy.

Metabolic Flux Model to Optimize *n*-butanol Production by *Clostridium tyrobutyricum*

Sarah McFann, Lauren Mathews, Michael Leffler, Carson Dietrich, Anna Crumbley, Chao Ma, Margaret Liu

Faculty Mentor: Margaret Liu – 205-348-0868 – mliu@eng.ua.edu

Department of Chemical and Biological Engineering, The University of Alabama, Tuscaloosa, Alabama 35487

Though biobutanol is a promising alternative fuel source due to its high energy content, compatibility with combustion engines, and blending ability, it is currently more expensive to produce than gasoline. However, metabolic engineering strategies can be used to optimize bacterial strains for butanol fermentation, thereby increasing the efficiency of biomass conversion to butanol and decreasing the cost of butanol production. In this study, a constraint-based metabolic model of *Clostridium tyrobutyricum* was developed to identify an engineering strategy for redirecting *C. tyrobutyricum* carbon flux to butanol synthesis while maintaining the energy and reducing power generation necessary for cell survival. The model was validated with experimental data and a strategy for maximizing butanol production was determined.

Introduction

Fluctuating crude oil prices and growing concern over both national security and the environmental impact of burning crude oil have necessitated the development of alternative fuel sources. Biobutanol (*n*-butanol produced by fermentation) shows promise as a substitute for petroleum-based fuel owing to its high energy content, compatibility with combustion engines, and blending ability. Additionally, net greenhouse gas emissions from burning butanol are near zero because the CO₂ emitted during butanol consumption is recycled in synthesizing biomass for fermentation [1]. However, high production costs currently make butanol an expensive alternative to traditional fuel.

Fortunately, metabolic engineering strategies can be used to optimize bacteria for butanol production, thereby decreasing the cost of biobutanol. Though *Clostridium acetobutylicum* was the first microorganism employed to synthesize butanol by fermentation, this bacterium's native butanol pathway is associated with sporulation and cell autolysis, which makes optimization by metabolic engineering difficult [2]. *Clostridium tyrobutyricum*, like *C. acetobutylicum*, is Gram-positive, anaerobic, and acidogenic, but unlike *C. acetobutylicum*, *C. tyrobutyricum* is not solventogenic and does not natively produce butanol. The metabolic activities of *C. tyrobutyricum* naturally create a strong driving force for butyric acid production, however, and when a butanol synthesis pathway is introduced into the bacteria, this driving force pushes butanol synthesis forward [3]. Therefore, *C. tyrobu-*

tyricum shows promise for economical butanol production.

Using flux balance analysis (FBA), a constraint-based metabolic model of *C. tyrobutyricum* can be constructed to identify which enzymes should be regulated for optimal butanol production by the microorganism [4]. A constraint-based metabolic model is an idealized view of the cell that represents the cell's metabolic pathways as a nodal network. A metabolite can be visualized as flowing down an edge of the network until it reaches a node, at which point the metabolite is converted stoichiometrically into a different metabolite, as shown in Fig. 1. If the node sits at the juncture of more than two edges, the flow, or flux, of the new metabolite can be distributed among the edges in a number of ways.

A bacterial cell directs its fluxes differently depending on the growth environment, the point in the

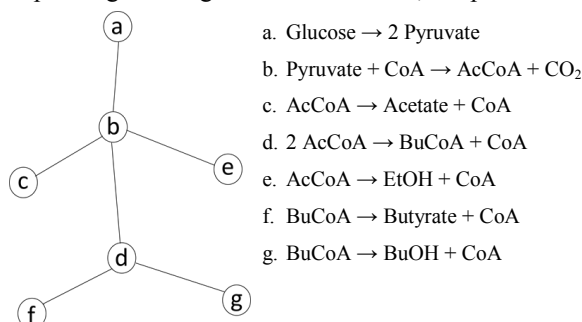


Figure 1. An example nodal network. Metabolites flow down the edges of the network until they encounter a node, at which point the metabolites undergo the chemical reaction corresponding to that node and are converted stoichiometrically into different metabolites.

cell cycle, and the pathways that are artificially regulated. To accurately simulate how a microorganism will distribute its fluxes in a given circumstance, an appropriate objective function, or equation with variables to be maximized or minimized given certain constraints, must be chosen. The objective function is a mathematical representation of the physical objective of a cell, and the constraints of the objective function can be derived from reasonable physical assumptions.

The goals of this study were to use experimental and computational methods to determine the metabolic flux distributions in ACKKO-*adhE2* (a *C. tyrobutyricum* strain) in free-cell fermentation with a bioreactor, to identify how flux could be redistributed to improve butanol yield, and to identify what factors most limit butanol production by *C. tyrobutyricum*.

3. Experimental Design

3.1. Strain and Media

The mutant ACKKO-*adhE2* analyzed in this study was constructed from the *C. tyrobutyricum* ATCC 25755 strain by downregulating acetate kinase (*ack*) to enhance C4 selectivity and by overexpressing the heterologous gene coding for bifunctional aldehyde/alcohol dehydrogenase (*adhE2*) to introduce a butanol synthesis pathway [2, 5]. The seed culture was maintained anaerobically at 37°C in Reinforced Clostridial Medium (RCM; Difco, Kansas City, MO) supplemented with 30 µg/mL of erythromycin and 30 µg/mL of thiamphenicol. Clostridial Growth Medium (CGM) was used to cultivate the cells in fermentation, as previously described [6, 7].

3.2 Bioreactor Culture

The free-cell fermentation was performed in a stirred-tank bioreactor (FS-01-A; Major Science, Saratoga, CA). After autoclaving at 121°C for 60 minutes, the fermentation medium was sparged with nitrogen gas at a flow rate of 10 mL/min for 3 hours to reach anaerobiosis. The bioreactor contained 2 liters of CGM, ~40 g/L glucose, and 30 µg/mL of thiamphenicol. Fresh seed culture with an optical density at 600 nm (OD₆₀₀) of 1.5 was used to inoculate the 2 liter fermentation medium to reach a seeding density at OD₆₀₀ of ~0.04, with one unit of OD₆₀₀ corresponding to 0.38 g-dry cell/L [8]. The fermentation operated in fed-batch mode at 37°C, 100 rpm, and pH controlled at 6.0 ± 0.1 with 5 N NaOH. When the sugar level in the fermentation broth decreased below 10 g/L, concentrated glucose stock (400 g/L) was added. Fermentation was stopped when glucose was no longer being consumed by the microorganism.

3.3 Analytical Methods

The cell density was monitored by measuring the OD₆₀₀ of cell suspension using a spectrophotometer (Biomate3; Thermo Fisher Scientific, Waltham, MA). The concentrations of butanol, butyric acid, ethanol, and acetic acid were analyzed using high performance liquid chromatography (HPLC; Shimadzu, Columbia, MD).

3.4 Model Construction

A stoichiometric matrix, **S**, was constructed to mathematically represent the set of chemical reactions composing the central metabolism of *C. tyrobutyricum*. Each of the rows of the matrix corresponded to a chemical species present in the bacterial cell while each column corresponded to a reaction occurring in the cell. Entries of the matrix were stoichiometric coefficients. Columns were added to the matrix to represent the transportation of glucose into the cell and the transportation of acetic acid, butyric acid, ethanol, and butanol out of the cell. Two additional columns were added to represent biomass synthesis and biomass “exportation”, since biomass was produced by the cell but not consumed by it. The microorganism was assumed to operate at steady state, so the product of the stoichiometric matrix and the flux vector containing all of the unknown fluxes, **v**, was set equal to zero (**Sv** = 0), forming a linear programming problem (LP) as shown in Fig. 2.

A wide variety of microorganisms synthesize biomass with a similar weight fraction of carbon, re-

- a. Glucose → 2 Pyruvate
- b. Pyruvate + CoA → AcCoA + CO₂
- c. AcCoA → Acetate + CoA
- d. 2 AcCoA → BuCoA + CoA
- e. AcCoA → EtOH + CoA
- f. BuCoA → Butyrate + CoA
- g. BuCoA → BuOH + CoA

$$\begin{array}{c}
 \downarrow \\
 \left(\begin{array}{cccccccc|cccc}
 -1 & 0 & 0 & 0 & 0 & 0 & 0 & 0 & 1 & 0 & 0 & 0 & 0 & 0 \\
 2 & -1 & 0 & 0 & 0 & 0 & 0 & 0 & 0 & 0 & 0 & 0 & 0 & 0 \\
 0 & 1 & -1 & -2 & -1 & 0 & 0 & 0 & 0 & 0 & 0 & 0 & 0 & 0 \\
 0 & 0 & 0 & 1 & 0 & -1 & -1 & 0 & 0 & 0 & 0 & 0 & 0 & 0 \\
 0 & 0 & 1 & 0 & 0 & 0 & 0 & 0 & 0 & -1 & 0 & 0 & 0 & 0 \\
 0 & 0 & 0 & 0 & 1 & 0 & 0 & 0 & 0 & 0 & -1 & 0 & 0 & 0 \\
 0 & 0 & 0 & 0 & 0 & 1 & 0 & 0 & 0 & 0 & 0 & 0 & -1 & 0 \\
 0 & 0 & 0 & 0 & 0 & 0 & 1 & 0 & 0 & 0 & 0 & 0 & 0 & -1
 \end{array} \right) \begin{array}{c} v_1 \\ v_2 \\ v_3 \\ v_4 \\ v_5 \\ \vdots \\ v_{12} \end{array} = \begin{array}{c} 0 \\ 0 \\ 0 \\ 0 \\ 0 \\ 0 \\ 0 \\ 0 \end{array}
 \end{array}$$

Figure 2. The conversion of a list of chemical reactions (from the example network of Fig. 1) into a stoichiometric matrix, and the formation of an LP (**Sv** = 0). While the stoichiometric matrix corresponds to the reactions occurring at the nodes of the network, the flux vector is related to the metabolite flow along the edges of the network. Entries to the right of the line partitioning the stoichiometric matrix represent the transportation of metabolites into and out of the bacterial cell.

tion of biomass from glucose [9]:



The stoichiometric coefficients from Eq. 1 were used for the biomass entry in the stoichiometric matrix. The molecular formula reported for the biomass of wild type *C. tyrobutyricum* was used to produce an estimate for the molar weight of ACKKO-*adhE2* biomass and to determine the subscript values for the biomass molecular formula in Eq. 1 [10]:



The stoichiometric matrix was constrained by the assumption that production and consumption of NADH/NADPH and ATP (cofactors that provide the bacterial cell with reducing power and energy, respectively) were balanced, since non-availability of these cofactors would limit which functions could be performed by the bacterial cell. Additionally, transient state and long-term variations in enzyme concentrations were not taken into account when developing the model because product secretion measurements were taken on a time scale of minutes [11]. A standard linear optimization algorithm was used to determine which flux distribution satisfied the butanol objective function.

4. Results

4.1 Acid & alcohol production and cell growth

By the end of the fermentation (78 hours), butanol concentration had reached a maximum value of 16.9 g/L and the concentrations of butyric acid, acetic acid, and ethanol were 4.2 g/L, 0.5 g/L, and 1.3 g/L, respectively. Unlike acetone-butanol-ethanol (ABE) fermentation by *C. acetobutylicum*, in which the microorganism synthesizes solely acetic acid and butyric acid (acidogenesis) in early fermentation and then switches to butanol and ethanol synthesis (solventogenesis) in late fermentation, ACKKO-*adhE2* showed no distinct acidogenic phase. Rather, as shown in Fig. 3, ACKKO-*adhE2* simultaneously produced solvents and acids from the beginning of the exponential phase and then shifted to solventogenesis at 54 hours.

ACKKO-*adhE2* grew with a lag phase of ~20 hours and had a specific growth rate of 0.16 h⁻¹ with a total fermentation timeline of 90 hours. The biomass yield was 0.06 g/g-glucose.

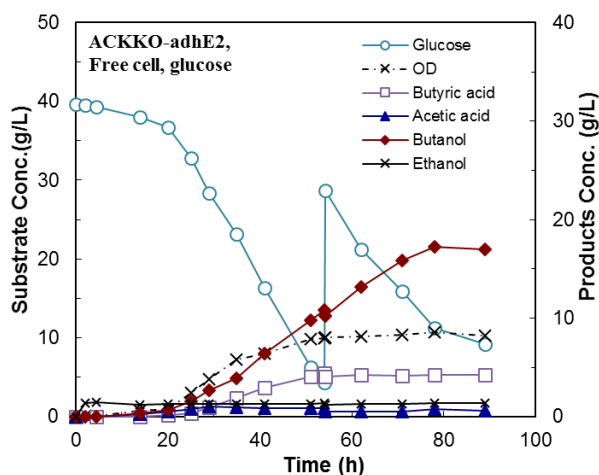


Figure 3. Glucose consumption, cell growth, acid synthesis, and solvent synthesis by ACKKO-*adhE2*.

4.2 Flux Balance Analysis of Butanol Production by *C. tyrobutyricum*

The metabolic flux distribution that maximized butanol production, under the assumption that NADH/NADHP and ATP production equaled consumption, was obtained from the solution to the LP problem with butanol as the objective function. Table 1 includes the acid, solvent, and biomass yields from the simulation results.

The LP problem solution (column B in Table 1) resulted in a flux distribution with a theoretical butanol yield of 0.851 mol/mol-glucose, achieved by halting ethanol and hydrogen production and redirecting excess carbon flux—carbon flux not directed toward butanol or biomass synthesis—toward acetic acid synthesis. This optimal butanol yield surpassed the experimental ACKKO-*adhE2* yield of 0.73 mol/mol-glucose by 17%.

	Yield (mol/mol-glucose)				
	A	B	C	D	E
Acetic acid	0.027	0.053	0	0.029	0
Butyric acid	0.155	0	0.053	0	0.029
Ethanol	0.091	0	0	0	0
Butanol	0.730	0.851	0.825	0.918	0.903
Biomass	0.101	0.183	0.183	0.101	0.101

Legend: A = ACKKO-*adhE2* experimental data, B = LP problem solved with butanol as the objective function (BOF), C = BOF, acetic acid synthesis halted (AASH), D = BOF, ATP generation allowed to exceed consumption (ATPE), E = BOF, AASH, ATPE.

Table 1. Experimental and theoretical acid, solvent, and biomass yields by *C. tyrobutyricum*.

When the equations representing the chemical reactions in the acetic acid synthesis pathway were removed from the LP problem to simulate *ack* down-regulation in ACKKO-*adhE2* and the problem was solved with butanol as the objective function, butanol yield was 0.825 mol/mol-glucose. This yield (column C in Table 1) was achieved when ethanol and hydrogen production were halted and excess carbon flux was directed toward butyric acid synthesis. Though lower than when the acetate synthesis pathway was left intact, this optimal butanol yield surpassed the experimental ACKKO-*adhE2* yield by 13%.

In order to compare the distribution of carbon flux, reducing power, and energy between simulation results and ACKKO-*adhE2* experimental data, the internal flux distribution of ACKKO-*adhE2* had to be calculated. The experimental yields of ethanol, butanol, acetic acid, and butyric acid by ACKKO-*adhE2* (column A in Table 1) were input into the general LP problem as the amount of solvent, acid, and biomass transported out of the cell. Before solving the problem, it was noted that the experimental biomass yield was much smaller than the biomass yield predicted by the simulation in all cases, 0.101 versus 0.183 mol/mol-glucose. Interestingly, although reducing power and carbon flux were easily balanced, the LP problem could only be solved when ATP production was allowed to exceed ATP consumption.

This result implied that ATP production could be allowed to exceed ATP consumption in the constraint-based model and that a higher optimal butanol yield was likely possible. The LP problem with butanol as the objective function was solved again, this time with biomass yield set at 0.101 mol/mol-glucose, as in the experimental data. Here (column D in Table 1), a maximum butanol yield of 0.918 mol/mol-glucose was achieved by halting ethanol and hydrogen synthesis, surpassing the experimental ACKKO-*adhE2* yield by 26%. When the problem was solved analogously with no acetate synthesis (column E in Table 1), the maximum butanol yield achieved was 0.903 mol/mol-glucose, surpassing the ACKKO-*adhE2* yield by 24%.

5. Discussion

These results provided insight into how carbon flux, reducing power, and energy were distributed in ACKKO-*adhE2* and how redistribution of these fluxes could improve butanol production.

Carbon flux from glucose consumed by *C. tyrobutyricum* was split between acid production, solvent production, and biomass maintenance. As shown in Fig. 4, biomass maintenance required ATP, which was supplied through glycolysis as well as acetic acid and butyric acid synthesis.

The acetic acid pathway generated the same amount of ATP as the butyric acid pathway using only half the carbon flux. Thus, butanol yield was optimized in the simulation by conserving carbon flux through utilization of the acetic acid pathway for ATP regeneration. This can be seen in Fig. 5, where the flux distributions of simulated bacteria employing

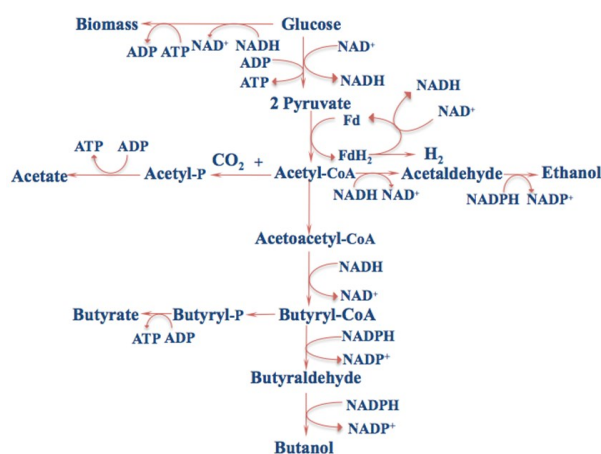


Figure 4. Central metabolism of *C. tyrobutyricum*.

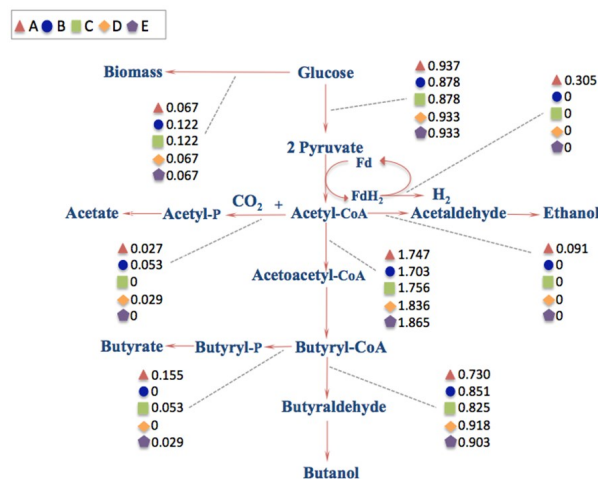


Figure 5. *C. tyrobutyricum* experimental and optimal flux distributions on a basis of 1 mole glucose. Legend: A = ACKKO-*adhE2* experimental data, B = LP problem solved with butanol as the objective function (BOF), C = BOF, acetic acid synthesis halted (AASH), D = BOF, ATP generation allowed to exceed consumption (ATPE), E = BOF, AASH, ATPE.

either the acetic acid pathway (B, D) or the butyric acid pathway (C, E) are both shown.

Utilization of the acetic acid synthesis pathway for ATP generation could be implemented experimentally by downregulating *ptb* in *C. tyrobutyricum*, an important enzyme in the butyric acid synthesis pathway, rather than downregulating *ack*, as was done in this study.

Butanol yield was further optimized in the simulation by conserving reducing power through the elimination of hydrogen synthesis. Reducing power was required for biomass, butanol, ethanol, and hydrogen synthesis, so halting hydrogen production allowed for the redistribution of reducing power. Due to the fact that no hydrogen gas was produced in the simulation when butanol production was optimized, it can be inferred that reducing power was limiting to butanol production. Therefore, butanol yield by *C. tyrobutyricum* in free-cell fermentation would likely increase if reducing power became more available. The experimental data indicated that the hydrogen gas yield of ACKKO-*adhE2* was 0.305 mol/mol-glucose. Any metabolic modification that decreased this yield would likely improve butanol production.

Butanol yield was further optimized in the simulation by conserving reducing power and carbon flux through the elimination of ethanol synthesis. Reducing power was required to convert acetyl-CoA into butyryl-CoA and butyryl-CoA into butanol, but was also necessary for the conversion of acetyl-CoA into ethanol. Reaction stoichiometry dictated that for every mole of ethanol produced, 2 moles of NADPH were required, and for every mole of butanol produced, 3 moles of NADPH and 1 mole of NADH were required. Because one mole of butanol contained four moles of carbon while one mole of ethanol only contained two moles of carbon, in both cases one mole of NADH/NADPH was required for every mole of carbon leaving the cell as solvent. Thus, the two processes were equally costly in reducing power, and halting ethanol production would conserve carbon and reducing power in equal measure.

Although experimental evidence indicated that ATP was not limiting for butanol production, ATP distribution greatly affected butanol production. Specifically, redistributing ATP consumption away from biomass synthesis in the simulation led to a large increase in butanol yield. As evidenced by the internal flux distribution of ACKKO-*adhE2*, much less biomass was necessary for proper cellular function than

the amount required to fully consume all of the ATP produced by the cell. For every unit of biomass foregone, carbon and reducing power became available for conversion into butanol. Therefore, determining how to achieve the minimum biomass yield necessary for proper cellular function would be a viable strategy for improving butanol yield. The fact that enough carbon flux could be sent down the acetic acid synthesis pathway to produce excess ATP also supported the hypothesis that reducing power was limiting to butanol production and not carbon.

6. Conclusion

In this study, a constraint-based metabolic model was constructed using flux balance analysis to calculate the internal flux distribution of ACKKO-*adhE2* from experimental data and to determine an optimal flux distribution for high butanol yield. Analysis of the experimental and computational results indicated that butanol yield could be improved by redirecting carbon flux from butyric acid to acetic acid synthesis, redistributing reducing power from hydrogen synthesis to butanol synthesis, and minimizing biomass yield. Additionally, it was determined that ACKKO-*adhE2* produced more ATP than it consumed in biomass synthesis and that reducing power was limiting for butanol synthesis by *C. tyrobutyricum*.

References

- [1] Dürre P. (2007). Biobutanol: an attractive biofuel. *Biotechnol. J.*, 12: 1525-1534.
- [2] Yu M, Zhang Y, Tang IC & Yang ST. (2011). Metabolic engineering of *Clostridium tyrobutyricum* for n-butanol production. *Metab. Eng.*, 13: 373-382.
- [3] Ma C, Kojima K, Xu N, Mobley J, Zhou L, Yang S & Liu X. (2015). Comparative proteomics analysis of high n-butanol producing metabolically engineered *Clostridium tyrobutyricum*. *J. Biotechnol.*, 193: 108-119.
- [4] Orth J, Thiele I & Palsson B. (2010). What is flux balance analysis? *Nat. Biotechnol.*, 28(3):245-248.
- [5] Liu X, Zhu Y & Yang ST. (2006). Construction and characterization of *ack* deleted mutant of *Clostridium tyrobutyricum* for enhanced butyric acid and hydrogen production. *Biotechnol. Prog.*, 22: 1265-1275.
- [6] Dong H, Tao W, Dai Z, Yang L, Gong F, Zhang Y & Li Y. (2012). Biobutanol. *Adv. Biochem. Eng. Biotechnol.*, 128: 85-100.
- [7] Jones SW, Tracy BP, Gaida SM & Papoutsakis ET. (2011). Inactivation of sigmaF in *Clostridium acetobutylicum* ATCC 824 blocks sporulation prior to asymmetric division and abolished sigmaE and sigmaG protein expression but does not block solvent formation. *J. Bacteriol.*, 193: 2429-2440.
- [8] Jaros AM, Rova U & Berglund KA. (2013). Acetate adaptation of clostridia tyrobutyricum for improved fermentation production of butyrate. *Springerplus*, 2: 47-54.
- [9] Papoutsakis ET. (1984). Equations and calculations for fermentations of butyric acid bacteria. *Biotechnol. Bioeng.*, 26: 174-187.
- [10] Song H, Eom MH, Lee S, Lee J, Cho JH & Seung D. (2010). Modeling of batch experimental kinetics and application to fed-batch fermentation of *Clostridium tyrobutyricum* for enhanced butyric acid production. *Biochem. Eng. J.*, 53: 71-76.
- [11] Durot M, Bourguignon PY & Schachter V. (2008). Genome-scale models of bacterial metabolism: reconstruction and applications. *FEMS Microbiol. Rev.*, 33: 164-190.

About the Author

Originally from Arlington, Tennessee, Sarah McFann is a junior in the Department of Chemical and Biological Engineering at The University of Alabama (UA). She is president of Omega Chi Epsilon, UA's chemical engineering honor society; president of Gamma Sigma Epsilon, UA's chemistry honor society; and publicity chair of UA's American Institute of Chemical Engineers (AIChE) chapter. Sarah has conducted research in Dr. Margaret Liu's lab since August 2014 and has previously conducted research under Dr. Daniel Fletcher at the University of California, Berkeley, Dr. Yohsuke Yamamoto at Hiroshima University, and Dr. Anthony Arduengo in UA's Chemistry Department. She is a Goldwater Scholar and an Amgen Scholar and has presented her work at the national AIChE student conference in Atlanta, Georgia, the regional AIChE student conference in San Juan, Puerto Rico, and the NanoBio Summit.

High Productivity, Serum-free, Suspension CHO Cell Culture Process Development for Anticancer Therapeutic Protein

Joanna Urli, Justine Panian, Emily Facchine, Michael Steadman, Brett Brankston, Theresa Borcky, Ningning Xu, and Margaret Liu

Faculty Mentor: Margaret Liu – 205-348-0868 – mliu@eng.ua.edu

Department of Chemical and Biological Engineering, The University of Alabama, Tuscaloosa, Alabama 35487

An effective, robust, and expandable CHO cell culture process was developed in this project to produce anticancer therapeutic proteins. CHO host cells, the predominant hosts in the biopharmaceutical industry, were adapted from adherent culture to suspension culture and afterwards from serum-dependent to serum-independent culture for improved growth and sustainability. The adapted cells exhibited desired growth in the successful cell cloning study, which was performed via limiting dilution. This serum-free suspension cell culture process can be used to effectively and quickly establish cell lines expressing anticancer therapeutic proteins and will help with future industrial manufacturing.

Introduction

As cancer causes millions of deaths every year, significant efforts have been made to develop effective anticancer therapies. While anticancer therapeutic proteins are one of the most remarkable medicines, capable of defeating many kinds of cancers and benefiting cancer patients, most of the current protein therapeutics are recombinant [1]. The CHO host cells are the most widely used hosts to express the recombinant anticancer therapeutic proteins, due to their adaptability of exterior DNA, their ease of maintenance, and the high quality of the proteins they express [2].

Three kinds of CHO host cells, CHO K1, CHO S, and CHO DG44 cells, were investigated in this study, as a number of CHO cell lines that express recombinant therapeutic proteins were developed from these lineages [3]. CHO K1 cells are the first parental CHO cells with reduced genome DNA. While most other CHO host cells have gone through an abundance of mutagenesis and/or kinds of selection, CHO DG44 hosts are metabolically engineered cells without the dihydrofolate reductase gene (dhfr) for easy selection and amplification of producing cell lines; CHO S hosts are well-adapted cells from original CHO cells with great cell growth. These three CHO hosts, derived from different lineages, have various effects upon the production of recombinant proteins and account for most of the phenotypic features, such as cell growth, cell lines' productivity, and proteins' quality.

CHO cells are originally adherent cells, but they are usually adapted into suspension culture. Adherent cell

growth is limited to the surface area, which restricts cells from growing to a higher cell density and to a large-scale culture. Suspension cells grow faster and have higher cell densities/viabilities, which are very helpful for efficient construction and easy scale-up of the cell lines in a bioreactor. Though the adaptation step is time-consuming, it is definitely considered to be beneficial.

The use of serum has its advantages: Serum is suitable for lots of cell lines and its included growth factors can definitely improve cell growth. However, there are many risks and high expenses for companies that use serum in the cell culture [4]. Serum is a poorly defined mixture, which increases the risk of introducing contaminants, including viruses, into cell culture and makes the isolation and purification of protein products extremely difficult. Additionally, the high cost of serum hinders its future use in industrial processes. Meanwhile, chemically defined media are being developed and used in large-scale processes, as they are economical and meet the Current Good Manufacturing Practices (cGMP) quality standard [5].

Materials and Methods

CHO Host Cell Culture

Three kinds of CHO host cells, CHO K1, CHO DG44, and CHO S, which have variable growth characteristics but are all popular hosts to express therapeutic proteins, were used in this project. These CHO host cells were first in adherent and serum-dependent growth, were cultured in T-flasks, and needed 10% serum in the corresponding media. After adaptation, the cells were in suspension culture in shake flasks and no serum was needed. Both the adherent cells and

	Serum-dependent cell culture	Serum-free cell culture
Composition	Poorly defined	Completely defined
Cell growth	Nutritious mixture to enhance cell growth	Specific formulations to support cell growth
Contamination	Great risk to introduce contamination, even viruses	Lower risk to introduce harmful agents
Production	Hamper product isolation and purification	Adapting cells into serum-free culture is time consuming
Economic efficiency	Higher cost	Lower cost

Table 1. Comparison of serum-dependent cell culture and serum-free cell culture

the suspension cells were incubated in a humidified environment with 5% CO₂ at 37°C. Only the adherent cell cultures were stationary, while the suspension cell cultures were on an orbital shaker rotating at 120 rpm.

Adherent Cell Culture

Adherent CHO cells were routinely passaged every 2-3 days. Adherent cells were first detached from the vessel using the enzyme trypsin and re-suspended in fresh medium. The cell density was determined using a hemacytometer, and the cell viability was tested through trypan blue dye exclusion. Afterwards, the seeding culture and the pre-warmed fresh medium were added into a T-flask according to the calculations to make a new cell culture at a cell density of 3x10⁵ viable cells/mL. The newly formed cell culture was incubated in a 37°C-humidified environment with 5% CO₂.

Suspension Cell Culture

Suspension CHO cells were passaged every 2-3 days in fresh medium in order to maintain or increase the density of healthy cultures. Before passage, the cell viability and density were calculated to determine the amount of original culture and medium to be added. After this was done, the culture was seeded at a

density of 3x10⁵ viable cells/mL. The calculated amounts of pre-warmed medium and cell suspension were added into a 125-mL shaker flask that was incubated in a 37°C-humidified environment with 5% CO₂ on a shaker platform.

Cell Cloning by Limiting Dilution

Limiting dilution cloning was performed to study the growth features of CHO cells at a very low cell density in the microwell plates. The CHO K1/EPO cell pool was constructed using adapted CHO K1 host cells in our lab. The CHO K1 cell line is the ancestral cell line among these cell lines, and it is one of the most typical cell lines in the biopharmaceutical industry, so it is the only one used for this process. First, the CHOK1/EPO cells were passaged routinely to ensure high viability; meanwhile, conditioned medium was prepared using earlier CHO K1 cell culture. On the day of cloning, CHO K1/EPO cells were serially diluted with the prepared cloning medium and seeded 1 cell/well, 5 cells/well, 20 cells/well, and 100 cells/well in the 96-well plates. The seeded plates were incubated in a 37°C-humidified environment with 5% CO₂ for 14 days without any disturbance. After incubation, the wells were screened under a microscope to determine the survivability.

Results and Discussion

Adaptation to Suspension Culture

CHO host cells were successfully adapted from adherent growth to suspension growth in this study. Figure 1 shows the viable cell density (VCD) and the cell viability during the adaptation process. Parental CHO DG44 cells are the most difficult to adapt, while CHO S cells are the easiest to adapt. Twenty-one days were spent to adapt CHO K1 cells, and the cell density was lower than 2x10⁶ cells/mL

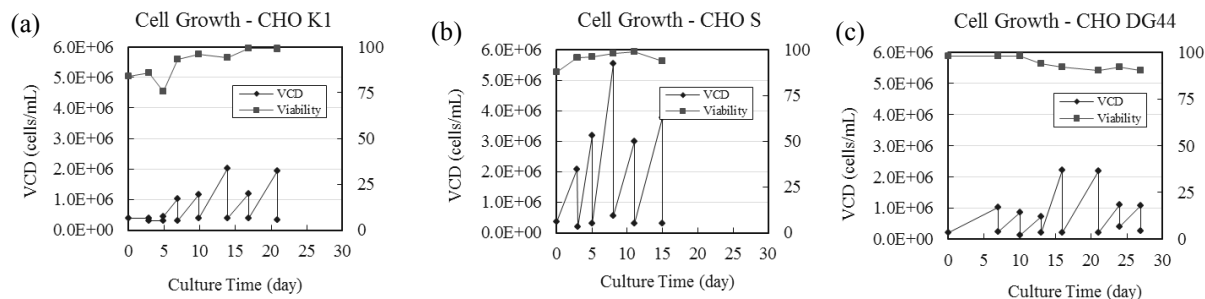


Figure 1. CHO host cell were adapted from adherent growth to suspension growth. The CHO K1 cell growth during adaptation is shown in (a), the CHO S cell growth during this process is presented in (b), and the cell growth of CHO DGG44 cells is exhibited in (c).

during the 2-3 days routine passage. However, only fifteen days were needed to adapt CHO S cells from adherent cells to suspension cells, and the maximum cell density was 5.6×10^6 cells/mL. As for the CHO DG44 cells, twenty-seven days were used to finish the adaptation work, and the highest cell density was only 2.2×10^6 cells/mL. These results are consistent with the CHO host cell characteristics.

From Figure 2, it is easy to see the changes in cellular morphology before and after cell adaptation to suspension growth. Adherent cells spread on the surface of their container. Their cell density is lower than that of suspension cells. Also, when compared to the original adherent cells, the doubling time of adapted suspension cells is shorter, and the maximum cell density of adapted suspension cells is higher. The adapted cells were used for future studies, cell line development, and process optimization.

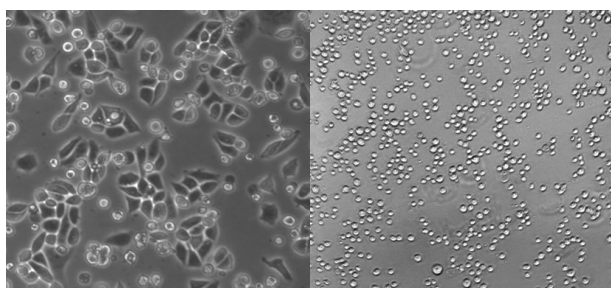


Figure 2. Cellular morphology of CHO host cells: adherent cells (left), suspension cells (right)

Adaption to Serum-Free Media

CHO cells were adapted from serum-dependent media to serum-free media by gradually removing the serum. The concentration of fetal bovine serum (FBS) was reduced from 10.0% to 5.0% on Day 7, and then the serum was completely removed from the culture on Day 10. After the serum was removed, the cells needed time to recover to reach the proper viable cell density. Essential processes such as scaling up the cell culture and banking cells usually follow the adaptations. The process took one month, as shown in Figure 3. The most important thing to note here is that the CHO K1 cells and CHO S cells are easily adapted into serum-free medium. Their adaption processes to serum-free media were combined with the adaption processes to suspension culture, studied in the above section.

Cloning Efficiency of Serum-Free Medium

After the CHO host cells were adapted into suspension and serum-free culture, they were used to construct clones. Again, CHO K1/EPO cells are the only cells used, because CHO K1 is the ancestral cell line among

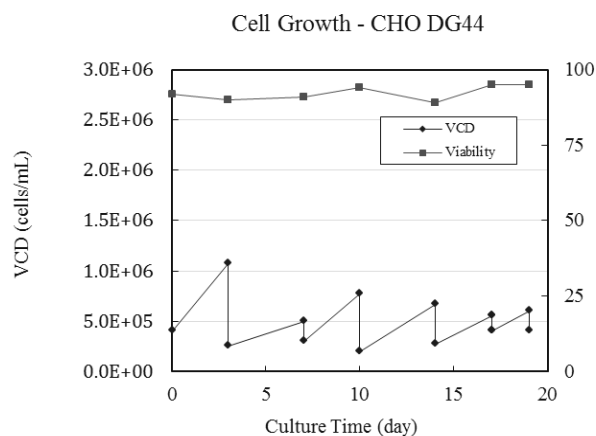


Figure 3. CHO DG44 cells were adapted to serum-free medium

the ones used. CHO K1/EPO cell pools are created via transfection of adapted CHO K1 cells with plasmid DNA. This CHO K1/EPO cell pool was used to perform cell cloning, in which the cells were diluted and seeded into 96-well plates at the cell density of 1 cell/well, 5 cells/well, 20 cells/well, and 100 cells/well. The ability of single-cell suspension growth is critical to recombinant protein production expressed in CHO cells, as it helps to obtain homogeneous and reliable protein products. However, it is usually a challenge for the cells to grow greatly at such a low density [6].

As shown in Figure 4, it was found that the CHO K1/EPO cell pool has very high cloning efficiency. Even for the lowest seeding cell density of 1 cell/well, 16.7% of wells showed clones. For the wells with seeding density of 5 cells/well, more than half of the wells grew clones. When the seeding density was higher than 20 cells/well, all the wells were found with clones. These results show that the CHO host cells

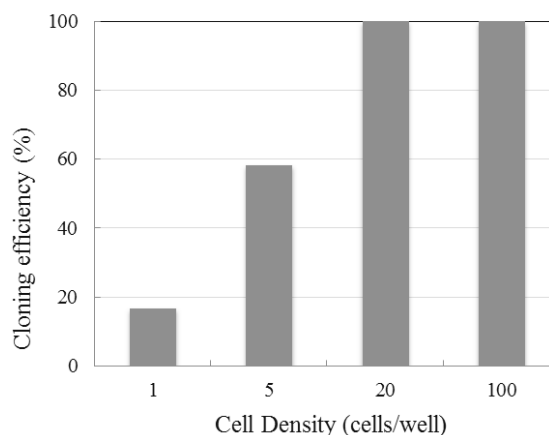


Figure 4. Cloning efficiency of CHO K1/EPO cells

were adapted successfully with improved cell growth, which will help to facilitate future studies.

Conclusion

Three kinds of the most popular CHO host cells were successfully adapted from adherent growth to suspension growth in order to overcome the limitation of growth areas and meet the large-scale manufacturing requirement. The serum was also completely removed from the suspension cell culture to reduce the risk of introducing harmful reagents into the cell culture. These adapted cells have been used to efficiently construct the CHO K1/EPO cell pool. The cell cloning was further performed using the constructed cell pool. The results showed that the adapted CHO cells had great growth even at a density of 1 cell/well. This study established cell lines that can be used in industrial manufacturing in the future.

References

- [1] Zhou LF, Xu N, Sun Y, Liu XM. (2014). Targeted biopharmaceuticals for cancer treatment. *Cancer Letters*, 352:145-151.
- [2] Jayapal KP, Wlaschin KF, Hu WS. (2007). Recombinant protein therapeutics from CHO cells: 20 years and counting. *Chemical engineering progress*, 103.10:40-47.
- [3] Lewis NE, Liu X, Li Y, Nagarajan H, Yerganian G, O'Brien E, Bordbar A, Roth AM, Rosenbloom J, Bian C, Xie M, Chen W, Li N, Baycin-Hizal D, Latif H, Forster J, Betenbaugh MJ, Famili I, Xu X, Wang J, and Palsson BO. (2013). Genomic landscapes of Chinese Hamster Ovary Cell lines as revealed by the *cricketulus griseus* draft genome. *Nature Biotechnology*, 31:759-765.
- [4] Sinacore MS, Drapeau D, and Adamson SR. (2000). Adaptation of mammalian cells to growth in serum-free media. *Molecular Biotechnology*, 15: 249-257.
- [5] Jerums M and Yang X. (2005). Optimization of cell culture media. *BioProcess International*, supplement: 38-44.
- [6] Ozturk SS, Palsson BO. (1990). Effect of initial cell density on hybridoma growth, metabolism, and monoclonal antibody production. *Journal of Biotechnology*, 16 (3-4): 259-278.

Acknowledgements

This work was supported by the Research Grant Committee (RGC), a grant from the Department of Chemical and Biological Engineering, and funding by the National Science Foundation (BRIGE 24512).

About the Author

Originally from Massapequa, New York, Joanna Urli is a sophomore in Chemical Engineering at The University of Alabama. She has been working in Dr. Margaret Liu's lab for one and a half years. She presented her research at the AIChE National Conference in Atlanta, Georgia in November 2014. She would like to thank Dr. Liu and Ningning Xu for their patience and support.

Digitizing the Algal Herbarium at The University of Alabama (UNA)

Joseph Cardosi, Joshua Blackwell, Frederik Leliaert Ph.D., Steve Ginzburg Ph.D., Juan Lopez-Bautista Ph.D.

Faculty Mentor: Juan Lopez-Bautista – jlopez@ua.edu

Department of Biological Sciences, The University of Alabama, Tuscaloosa, Alabama 35487

The University of Alabama Herbarium (UNA) contains well over 70,000 specimens of vascular plants, mosses, liverworts, lichens, algae, and fungi. To increase accessibility of the algal samples within the herbarium, digitization of current vouchers was done and made publicly accessible. Prior to this project, the only approach to obtain information regarding algal specimens contained within The University of Alabama Herbarium (UNA) was through physical examination or direct contact with the curator or collections manager. After successful digitization of over 1,600 algal samples, anyone interested in obtaining information for geographic, morphological, or even molecular studies on the vouchers can now easily access this information through the web.

Introduction

Natural history collections are a valuable asset to the scientific community. Across the world, more than a billion biological specimens have been preserved among collections and contained within museums, herbaria, and universities. Algal herbaria provide vast pools of specimens that can contribute to the identification and classification of specimens, as well as act as a record of morphology, evolution, and geographical distribution of species [1]. Specimens within herbaria can also be used to obtain molecular data for phylogenetic purposes, in particular for the elucidation of the Tree of Life [9].

Historically, access to samples within herbaria has been a difficult problem. Voucher specimens were only available through scheduled visits to the herbaria and by direct handling of the specimens. These factors can limit the accessibility to the herbarium itself and may damage the delicate specimens. Only by making collections widely accessible can they become real tools for researchers, educators, and students [8]. Digitization and online distribution of samples provides an excellent solution for increasing availability and accessibility of samples to the world. With their many significant uses, it is vital that the resources of The University of Alabama collections be made available to the public through modern methods such as digitization.

Prior to the current project, no reports were known regarding the algal collection contained within The University of Alabama Herbarium (UNA); however, earlier reports on Alabamian algae are known

[10]. The University's collection contains hundreds of specimens corresponding to green, red, and brown algae, including many deep-water specimens (greater than 50m deep) from the Gulf of Mexico.

These collections are especially significant in the study of shifts in species' distributions resulting from increased anthropogenic activity or relating to global climate change [5]. In addition, these collections are useful for verification of species introductions [6]. Some species have been reported as recent introductions (non-native species) into the Gulf of Mexico; this is the case of the red alga *Grateloupia taiwanensis*, reported recently from the Alabama Coast [3].

The goal of this project is two-fold: first, to electronically database information, along with a barcode, relating to each algal specimen within The University of Alabama Herbarium, and second, to digitize each specimen using high resolution photography and to make this imaging available through a web interface. This information will be accessible through the University's herbarium website (www.bama.ua.edu/~bsc/herbarium), the Global Biodiversity Information Facility [11] website, and through the recently formed partnership at the Macroalgal Herbarium Portal (www.macroalgae.org).

Methods

The University of Alabama Herbarium (UNA), housed at Mary Harmon Bryant Hall, contains over 70,000 specimens, including algae, bryophytes, ferns, gymnosperms, and angiosperms. Each algal

sample was set aside in order to be digitally recorded within the UNA system. The University of Alabama collections system utilizes Microsoft Access 2007 to keep records of all its specimens. Before any information regarding the algal specimen within the herbarium could be incorporated into this database, the names of over 73,000 extant algal genera and their families were added to the database's list of entries from *algaebase.org* [4].

Once the familial and generic information was added to the UA database network, we began cataloging each specimen. All available information was entered individually for each specimen and collection event. Each specimen was assigned a unique UNA barcode that can be used for convenient reference. Information such as the date that the specimen was collected, the locality of the collecting site, depth below sea level, Global Positioning System data (GPS), and other observations about the specimen were included for each voucher. In addition, data such as the identity of collectors and identifiers was also listed (**Figure 1**). Once herbarium specimens were barcoded and the database entry finalized, the specimens were mailed to The University of North Carolina Herbarium (NCU) for digitization. *The Macroalgal Herbarium Consortium: Accessing 150 Years of Specimen Data to Understand Changes in the Aquatic Environment* is an NSF funded project and was developed to image, database, and georeference macroalgal specimens in 49 herbaria, including UNA, from the continental USA as well as Hawaii and Guam [7]. Each specimen was digitally scanned and all pertinent information recorded.

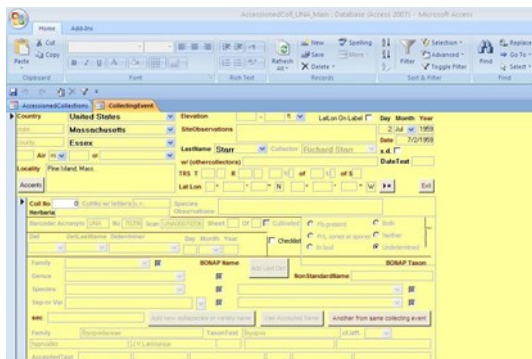


Figure 1. The University of Alabama Collections database details a wide variety of information for each of its over 78,000 specimens.

Results

Upload conversion of physical information from the herbarium voucher to digital data started in January 2014 and it was completed in September 2014. The digitized algal collection at UNA contains a variety of taxonomic groups belonging to several lineages including the green algae (Chlorophyta), red algae (Rhodophyta), brown algae (Phaeophyceae) and the blue-green algae (Cyanobacteria). The best-represented regions are from the Gulf of Mexico and the Florida Middlegrounds. Most algae contained at UNA are from the USA, and besides the North American continent, other regions are represented as well, such as South America (Brazil, French Guyana, Chile), Central America (Panama, Nicaragua), Africa (Gabon), and Europe (Italy, Spain, Portugal).



Figure 2. *Anadyomene stellata*, identified by phycologist Sylvia Earle in 1975

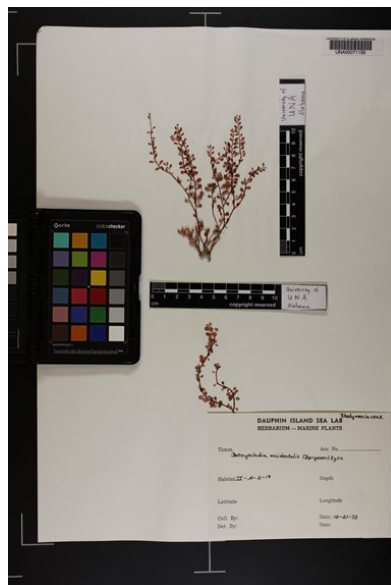


Figure 3. Example of a digitized specimen available from the Macroalgal portal website.

Each specimen held within UNA can now be accessed on the Macroalgal Herbarium Portal (www.macroalgae.org). Each voucher includes a high-resolution picture of the specimen as well as all information regarding the locality, habitat, and collection dates. The total number of algal specimens entered into the UNA database is 1,608 specimens (as of February 4, 2015). Currently this algal collection dates back nearly 100 years with the oldest algal specimen recorded in the University's collection dating back to the year 1919. A total of 69 families are representing ten countries on four continents. Many of these collections represent collective efforts of research projects during expeditions to the Gulf of Mexico. Among notable collectors for UNA we found phycologists such as Sylvia Earle (**Figure 2**) and Susan Brawley along with other scientists: Thomas S. Hopkins, Eric H. Livingston, Jay A. Shapiro, Diane E. Grimm, Charles H. Lutz, and Deborah R. Blizzard.

Conclusions

The University of Alabama Herbarium UNA contains algal specimens that are valuable for the purposes of identification and analysis of long-term changes in distribution patterns. These specimens provide a history of the evolution and geographical distribution of species. This is especially significant for the North Central Gulf of Mexico from which most of our collections are gathered, since this corresponds to an area subjected to anthropogenic disturbance such as the recent events of the BP Horizon oil spill [2].

The UNA utility continues to provide a valuable service to researchers, educators, and environmental managers. We have updated and barcoded all our collections into The University of Alabama Herbarium (UNA) database; we have also partnered with the initiative of Macroalgal Portal, and all our algal specimens have been digitally imaged at NCU and can be freely accessed from The Macroalgal Portal at www.macroalgae.org (**figure 3**). With this information widely available, anyone can access geographical and morphological information regarding the samples without the need to take a specimen loan out. Additionally, data mining from the UNA herbarium can now be done from the UNA database. Our successful digitization of UNA is one of 49 other herbaria that have partnered with the Macroalgal Herbarium Portal in order to begin the process of electronically sharing collection data with the public.

References

- [1]. Beaman R, Wieczorek J, & Blum S. (2004). Determining Space from Place for Natural History Collections. *D-Lib Magazine*. Vol 10(5):1082-9873
- [2]. Bik HM, Halanych KM, Sharma J, Thomas WK. (2012). Dramatic Shifts in Benthic Microbial Eukaryote Communities following the Deepwater Horizon Oil Spill. *PLoS ONE* 7(6): e38550. doi: 10.1371/journal.pone.0038550
- [3]. DePriest M, Lopez-Bautista J. (2012). Sequencing of the *rbcL* Marker Reveals the Nonnative Red Alga *Grateloupia taiwanensis* (Halymeniaceae, Rhodophyta) in Alabama. *Gulf of Mexico Science* (1-2):7-13.
- [4]. Guiry MD & Guiry GM. (2014). *AlgaeBase*. World-wide electronic publication, National University of Ireland, Galway. <http://www.algaebase.org>.
- [5]. Harley CDG, Hughes AR, Hultgen KM, Miner BG, Sorte CJB, Thorner CS, Rodriguez LF, Tomanek L & Williams, SL. (2006). The impacts of climate change in coastal marine systems. *Ecology letters* 9:228-241.
- [6] Harley CDG, Anderson KM, Demes KW, Jorge JP, Kordas RL & Coyle TA. (2012). Effects of climate change on global seaweed communities. *Journal of Phycology* 48:1064-1078.
- [7]. Schoonover K. (2015). University of Alabama Herbarium (UNA) Algae Collection: An Overview. *Phycological Newsletter* 51(1):21.
- [8]. Tegelberg R, Mononen T, & Saarenmaa H. (2014). High-performance Digitization of Natural History Collections: Automated Imaging Lines for Herbarium and Insect Specimens. *Taxon* 63(6):1307-1313.
- [9]. Thomas RH. (1994). Analysis of DNA from Natural History Museum Collections. *Molecular Ecology and Evolution: Approaches and Applications Experimentia Supplementum* 69:311-321.
- [10]. Mohr, C.T. (1901). *Plant Life of Alabama: An Account of the Distribution, Modes of Association, and Adaptations of the Flora of Alabama, Together with a Systematic Catalogue of the Plants Growing in the State*. Prepared in Cooperation with the Geological Survey of Alabama. Vol. 6. US Government Printing Office.
- [11]. GBIF (2015). Global Biodiversity Information Facility. Available online at www.gbif.org

Acknowledgements

We would like to thank Carol A. McCormick Curator at NCU for image processing of all our herbarium specimens; to National Science Foundation Assembling the Tree of Life and NSF Research Experience for Undergraduates (REU) programs (DEB 0937978 and DEB1036495) for funding to JLB.

About the Author

Originally from Fort Mitchell, Kentucky, Joseph Cardosi is currently a senior majoring in Biology at UA. He has been conducting research in Dr. Juan Lopez-Bautista's PhycoLab for over a year as a NSF/REU undergraduate researcher and BSC 398 for credits. In addition to his time spent in the lab, Joseph has given a presentation on this work at the Southeastern Phycological Colloquy (SEPC) at The University of North Carolina at Wilmington (October 2014) as well volunteers at a dental clinic in Northport, Alabama and hopes to attend School of Dentistry after graduating in 2015.

Joshua Blackwell, a biology major at UA participated in the PhycoLab taking credits in BSC 398. Joshua has been accepted in the program of the School of Medicine.

Ecological Determinants of Blood Glucose in the Diamondback Water Snake *Nerodia rhombifer*

Danny L. Laderberg

Faculty Sponsor: Dr. Stephen Secor

Department of Biological Sciences, Box 870344, The University of Alabama, Tuscaloosa, AL, 35487

The regulation of blood glucose is an important homeostatic process for any animal, especially those that consume meals rich in carbohydrates. For strict carnivores, the capacity to regulate glucose may be partly diminished because of the reduced need to control elevated blood glucose. To investigate natural variation in blood glucose for a strict carnivore, I examined the effects of sex, size, feeding, fasting, hydration state, and stress on the blood glucose of the diamondback water snake (Nerodia rhombifer). Baseline resting concentrations of blood glucose for the water snakes ranged between 30-40 mg/dL. I found no difference for recently captured snakes between males and females in blood glucose levels. Blood glucose was found to decrease as a function of body mass. Compared to glucose levels measured from snakes maintained at 30°C, levels declined significantly when snakes were maintained at lower temperatures (10° and 20°C). Feeding generated no significant increase in blood glucose concentrations, as levels remained constant (36-40 mg/dL) for three days postfeeding. Likewise, fasting for up to six months resulted in no significant fluctuation in blood glucose values. In response to eight days of dehydration, blood glucose levels increased by 50%. Normal levels were restored within six hours following access to water. Stress, induced by 90 seconds of agitation, resulted in a significant increase in blood glucose levels within four hours. Glucose levels remained elevated for the following eight hours and returned to baseline values by hour 29.

Introduction

One of the most important homeostatic processes of the body is the regulation of blood glucose levels. For humans and other animals, diverging from normal levels of blood glucose can lead to severe physiological problems. Levels too low (hypoglycemia) can lead to the loss of brain function, coma, and death, whereas levels too high (hyperglycemia) are the underlying cause of diabetes, currently one of the most prevalent diseases of mankind, especially in the southeastern United States [1]. The regulation of blood glucose is controlled by the interactions of two pancreatic hormones, insulin and glucagon [1]. Insulin induces the removal of glucose from the blood, whereas glucagon operates to keep blood glucose levels from getting too low (i.e., hypoglycemia) [1]. Together, these two hormones serve to maintain glucose levels within an optimal range for any animal.

The importance of regulating blood glucose is understandably paramount for herbivores (plant eaters) and omnivores (plant and meat eaters, like humans) given the higher quantity of carbohydrates (and hence glucose) in their diet. The quantity of carbohydrates within the natural diet correlates with the rate of glucose uptake by the intestines; which is highest for herbivores, followed by omnivores, and lowest

for carnivores [2]. However, is the tight regulation of blood glucose after feeding so necessary for strict carnivores (meat eaters) due to their low glucose intake? Given that there is no chance for diet-induced hyperglycemia (and hence diabetes), have strict carnivores lost (through evolutionary time) the capacity to lower blood glucose? An adaptive justification for losing this ability is that energy will be saved rather than being spent on tissues and cells necessary to lower blood glucose [3]. Alternatively, if the capacity to regulate blood glucose is highly conserved among vertebrates, then even strict carnivores will retain the ability to regulate blood glucose.

To examine these competing hypotheses, I am studying the capacity of a strict carnivore, the diamondback water snake (*Nerodia rhombifer*), to regulate blood glucose levels. The diamondback water snake feeds primarily on fish and therefore consumes very little glucose (only as glycogen stored in tissues) from its diet. Snakes are strict carnivores, diverging from an omnivorous lizard ancestor 120-140 million years ago [4]. Thus, for at least 120 million years there has been no selected need for snakes to retain the ability to lower blood glucose levels after feeding. However, snakes do secrete insulin and glucagon into their blood with feeding [5, 6]. Unknown is the bioactivity of snake insulin and whether it stimulates tissues to remove glucose from the blood.

There has been relatively little attention given to the study of blood glucose in snakes. It is largely unknown as to what extent blood glucose will vary either in natural situations or experimentally. As a first step to exploring the capacity of the diamondback water snake to regulate blood glucose, I am examining how their blood glucose concentrations vary under different natural conditions. The aim of this paper is to describe, analyze, and discuss variation in blood glucose of the diamondback water snake as a function of body size, sex, and temperature, and in response to feeding, fasting, hydration state, and stress.

Materials and Methods

Snakes and care

The diamondback water snake inhabits a variety of freshwater habitats in south-central United States and eastern Mexico and feeds predominately on fish [7] (Fig 1a). The water snakes used in this study were captured by hand at a commercial catfish farm in LeFlore County, Mississippi during the spring of 2013 and 2014. Snakes were maintained communally in large tanks (1000 L) at 25-27°C and fed catfish weekly with water always available. To obtain baseline data prior to experimentation, snakes were fasted for one week to ensure that blood glucose levels were not influenced by meal digestion. To measure blood glucose, I drew a small amount of blood (50 μ L) from the caudal vein using a 1-cc syringe (25 ga needle). Blood was then applied to the Clarity blood glucose test strip (Fig. 1B) and glucose concentration (mg/dL) were recorded from the Clarity blood glucose meter display (model DTG-GL2PLUS, Boca Raton, FL). The site where blood was drawn was then swabbed with alcohol. I examined the effects of sex and body mass on blood glucose levels using both male and female snakes. Studies exploring the effects of temperature, feeding, fasting, dehydration, and stress were conducted using only male snakes. Snake care and experimentation were conducted with approval from the University of Alabama Institutional Animal Care and Use Committee.

Baseline and effects of sex, body mass, and body temperature

To assess variation in baseline blood glucose and differences due to sex and body mass, we measured blood glucose of snakes soon after capture and at various time points (following a week of fasting) throughout the study. Male and female differences were examined using snakes captured on the same day in 2014 and measured several days later. Body mass effects were explored using 47 snakes ranging in mass



Figure 1: (A) Diamondback water snake (*Nerodia rhombifer*). (B) Drawing blood from the caudal vein of a diamondback water snake. Photo credit (A) http://en.wikipedia.org/wiki/Nerodia_rhombifer#mediaviewer/File:Daimondback_Watersnake.jpg, (B) Dr. Stephen Secor.

from 158 g to 1284 g. The influence of body temperature was determined from blood samples drawn from 10 male snakes after being maintained for four days each at 10°C, 20°C, and 30°C.

Effects of feeding, fasting, dehydration/rehydration, and stress

To examine the effects of feeding, baseline blood glucose was recorded from 12 snakes maintained at 30°C. Snakes were then fed catfish meals equaling in mass to 20% of snakes' body mass, and blood glucose was measured at 1, 2, 3, 4, and 6 days after feeding. For meals of this size, digestion is completed four to six days after feeding [8]. Fasting effects were explored by measuring blood glucose from snakes ($n = 5-11$) fasted for 2, 4, and 6 months. The effects of dehydration and rehydration were determined from eight snakes maintained at 30°C that, following baseline measurements, had their water removed for eight days with measures of blood glucose taken at days 4 and 8. Immediately following the 8-day measurement, snakes were given access to water with blood glucose measured 6 hours later and 4 days later. The response to stress (agitation) was determined by stimulating five snakes to crawl vigorously within a plastic bucket for 90 seconds and drawing blood 15 minutes, 2, 4, 6, 8, 12, 29, 58, and 73 hours after while being maintained at 30°C.

Data analysis

I used an analysis of variance (ANOVA) and regression analysis to examine the effects of sex and body mass on blood glucose. I used repeated-measures ANOVA to test the effects of temperature, time postfeeding, duration of fasting, hydration treatments, and time post-stress on blood glucose levels. I followed ANOVAs with pairwise mean comparison (Tukey-Kramer procedure) to test for significant differences between treatments and time points. The level of statistical significance is designated at $P < 0.05$.

Results*Effects of sex, body mass, and body temperature*

For recently captured snakes, I found no significant difference in blood glucose levels between males and females (Fig. 2). Plasma concentration levels several days after capture generally ranged between 30-40 mg/dL. I did observe a significant ($P < 0.005$, $r^2 = 0.166$) decline in baseline blood glucose as a function of body mass (Fig. 3). Noted, however, is an interaction with sex for this data set as smaller snakes were generally males (< 600 g) and the larger snakes, females (> 800 g). Blood glucose levels of water snakes varied ($P < 0.0002$) among temperature treatments. Compared to levels measured from snakes maintained at 30°C, both lower temperature treatments (10 and 20°C) resulted in significantly (P 's < 0.009) lower blood glucose levels (Fig. 4).

Effects of feeding, fasting, dehydration/rehydration, and stress

Feeding had no immediate effect on blood glucose levels, as levels remained consistent (36-40 mg/dL) for three days after feeding (Fig. 5). However, levels did significantly decline after day 3 (27-32 mg/dL). The duration of fasting did not significantly impact blood glucose levels (Fig. 6). Even after six months of fasting, snakes had maintained a steady concentration of blood glucose (30-40 mg/dL). Different hydration states did significantly ($P < 0.0006$) affect blood glucose levels. Following eight days without water, blood glucose levels had risen by 50% (Fig. 7). Rehydration (given access to water) restored baseline blood glucose levels within six hours (Fig. 7). A 90-second bout of agitation (i.e., stress) generated a significant ($P < 0.022$) increase in blood glucose levels within four hours (Fig. 8). Blood glucose remained elevated (mean 76-91 mg/dL) for the next eight hours (until hour 12), and returned to baseline levels by hour 29 (Fig. 8). Blood glucose levels remained low for the remaining 44 hours of the experiment.

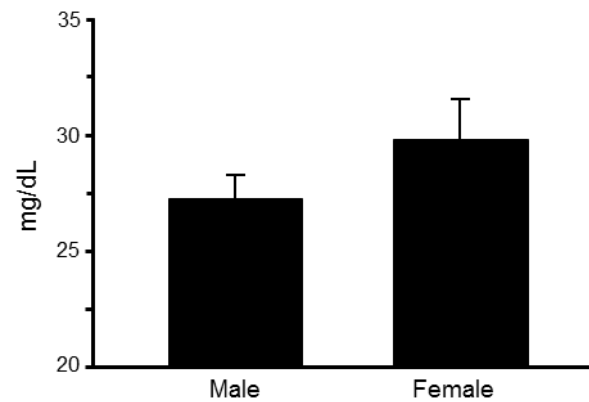


Figure 2: Mean (+1 SE) Baseline blood glucose concentration (mg/dL) of recently captured adult male and female diamondback water snakes. For this set of snakes, there was no difference in blood glucose.

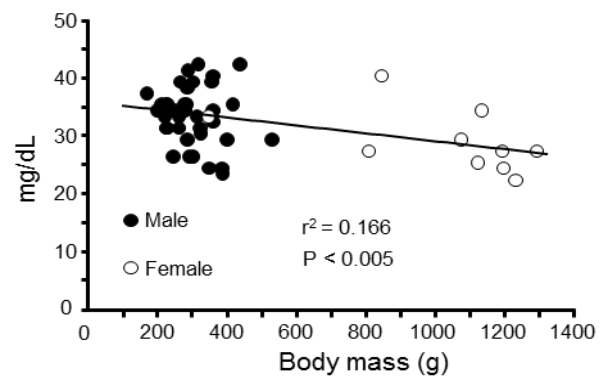


Figure 3: Baseline blood glucose concentration (mg/dL) plotted as a function of body mass for male (●) and female (○) diamondback water snakes. Note the decrease in blood glucose with increase body mass.

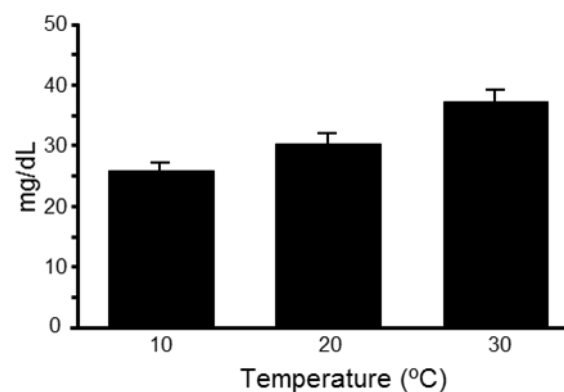


Figure 4: Mean (+1 SE) Blood glucose concentration (mg/dL) of diamondback water snake maintained at 10°C, 20°C, and 30°C. Note the increase in blood glucose with temperature.

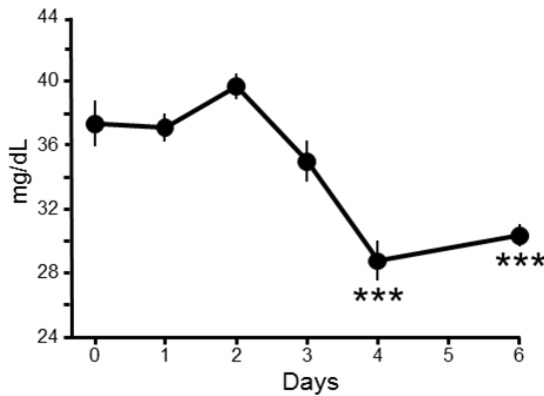


Figure 5: Mean (± 1 SE) Blood glucose concentrations (mg/dL) prior to (day 0) and following the consumption of a catfish meal equaling in mass to 20% of snake body mass for the diamondback water snake. Snakes exhibited a significant decrease (noted by ***) in blood glucose at day 4 and 5 after feeding.

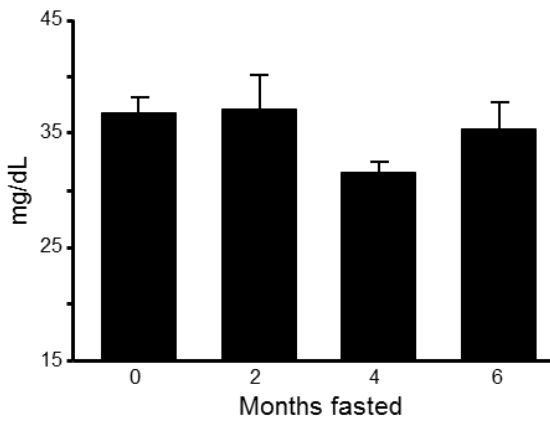


Figure 6: Mean (± 1 SE) Blood glucose concentrations (mg/dL) prior to (0) and following 2,4, and 6 months of fasting for the diamondback water snake. Snakes exhibited no differences in blood glucose levels over extended bouts of fasting.

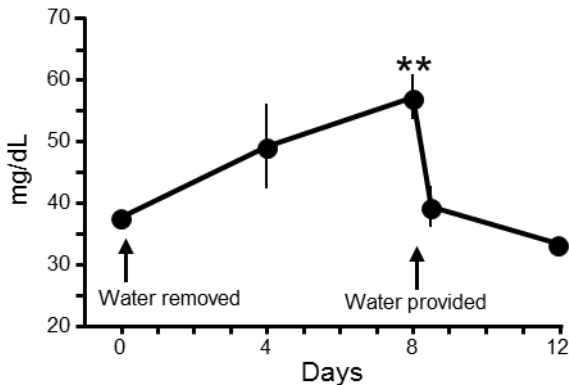


Figure 7: Mean (± 1 SE) Blood glucose concentrations (mg/dL) prior to (day 0), at 4 and 8 days of without access to water, and following access to water for the diamondback water snake. Snakes experienced a significant ($P < 0.007$) increase in blood glucose (noted by **) after 8 days without water. Blood glucose levels were restored within 6 hours after having access to water.

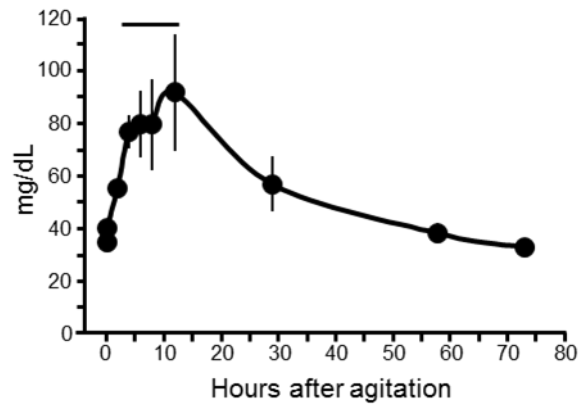


Figure 8: Mean (± 1 SE) Blood glucose concentrations (mg/dL) prior to (0) and following a 90-second bout of agitation for the diamondback water snake. Concentrations significantly increased within 4 hours and remained elevated (noted by solid line) before returning to baseline values by hour 29.

Discussion

Although a strict carnivore with very little sugar in its diet, the diamondback water snake must continue to maintain an adequate amount of glucose in its circulation. In nature there are potential abiotic and biotic factors that can influence blood glucose levels. The diamondback water snake experiences seasonal shifts in temperature, physiological changes with feeding and fasting, loss of body fluid with dehydration, and hormonal interactions that accompany stressful situations. For this study, I examined whether each of these natural events may possibly alter blood glucose levels for this snake. In the following I shall discuss the effects of sex, body size, feeding, fasting, hydration state, and stress on blood glucose concentrations of the diamondback water snake.

Baseline

The baseline values of blood glucose for the water snakes in this study generally ranged between 30-40 mg/dL. Our criteria for measuring baseline included snakes at rest, hydrated, and at least a week from the previous meal. The few studies that have documented blood glucose in snakes have reported varying baseline values. Reported mean values include 27 mg/dL for the puff adder (*Bitis arietans*), 45 mg/dL for Wagler’s snake (*Xenodon merremi*), 46 mg/dL for European grass snake (*Natrix natrix*), 55 mg/dL for the Burmese python (*Python molurus*), 56 mg/dL for the Brazilian pit viper (*Bothrops jararaca*), 59 mg/dL for the sand viper (*Cerastes ceras-tes*), 70 mg/dL for the boa constrictor (*Boa constrictor*), 106 mg/dL for the diamondback rattlesnake (*Crotalus atrox*), and 107 mg/dL for the Central

American coral snake (*Micrurus nigrocincius*) [9, 10, 11, 12, 13, 14, 15, 16]. Lacking from this data are any trends that can be affixed to phylogeny. While both *N. rhombifer* and *X. merrimi* are within the family Colubridae and exhibit similar blood glucose baselines, members of the family Viperidae (*Bitis*, *Bothrops*, *Cerastes*, and *Crotalus*) exhibit a wide range of blood glucose levels. In addition, variation among studies may also be attributed to the different methods used to collect blood (e.g., decapitation, cardiac puncture, and caudal vein) and analyze blood glucose levels (e.g., assay kits, autoanalyzer, blood glucose meter) [16].

Although we did not observe a significant variation in blood glucose between freshly-caught male and female snakes, sex did appear to potentially influence blood glucose given the significant relationship with body mass. Diamondback water snakes are sexually dimorphic with adult female snakes attaining body sizes two to three times larger than adult males. On average the larger adult females possessed lower blood glucose than the smaller adult males. Rather than consider a sexual difference between males and females in blood glucose, it appears that the observed relationship stems from the greater variability in baseline blood glucose levels for the smaller male snakes (Fig. 3). Measuring blood glucose from male and female snakes matched in body mass over a wider range of body masses would ascertain whether there are sex- or mass- related differences in blood glucose.

Body temperature

Diamondback water snakes experienced a decline in blood glucose when exposed to lower temperatures (10 and 20°C). Although temperature effects on blood glucose have not been directly explored for snakes, several studies have observed a decrease in blood glucose of snakes during winter dormancy (i.e., hibernation). The viperids, *Cerastes cerastes* and *Cerastes vipera*, experienced respective 42% and 56% decreases in blood glucose during the winter [9]. However, hibernation did not alter blood glucose of the viperid *Crotalus horridus* [17]. A decrease in body temperature lowers the snakes' metabolic rate and therefore their usage of glucose and glucose production. This may in part, explain the depression in blood glucose at the lower temperatures.

Feeding and fasting

Water snakes experienced no immediate change in blood glucose with feeding. While a post-feeding increase in blood glucose is characteristic for many animals, the lack of such an increase for the

snakes is undoubtedly due to the low carbohydrate content of their catfish meal. With very little glucose ingested, blood glucose levels remained steady. Additionally, a high protein meal is known to stimulate pancreatic release of insulin (which removes glucose from the blood) and glucagon (which preserves blood glucose)[1]. The actions of these hormones offset each other, and blood glucose remains stable. Feeding-induced release of insulin and glucagon has been documented for the Burmese python, which also does not exhibit a significant postprandial change in blood glucose [18, 6]. Likewise, feeding had no effect on blood glucose levels of the pit viper *B. jararaca*, which oscillates between 54-70 mg/dL for the week after feeding [14]. The significant drop in blood glucose observed after day 3 for the diamondback water snake is probably inconsequential, given that the values throughout the postfeeding period are within the range of baseline values (Fig. 5).

Even after months of fasting, water snakes were able to maintain their blood glucose levels. In the absence of feeding and a source of exogenous glucose (from meals), they maintain blood glucose by reducing the rate at which it is used and adding glucose to circulation by breaking down glycogen in the liver and manufacturing new glucose (i.e., gluconeogenesis). The snakes can synthesize new glucose from amino acids released from the breakdown of proteins, glycerol from the breakdown of triglycerides, ketones, and recycled lactate and pyruvate [19, 20, 21]. Similarly, extended periods of fasting for 20 and 24 weeks had no impact on the blood glucose values for the rattlesnake, *C. atrox* [12, 22]. Even eight months of fasting did not alter the blood glucose levels of the subterranean salamander, *Proteus anguinus* [23]. Ectotherms, due to their lower metabolic rate, appear to be more resilient to fasting-induced depression of the blood glucose levels.

Hydration state

The dehydration-induced increase in blood glucose levels might stem from two mechanisms. First, for the eight days without water, snakes lost on average 19% of their body mass, which is largely water. One source of that water is their plasma. As plasma decreases in water content, it increases in its concentrations of electrolytes and solutes, including glucose. In a separate study on diamondback water snakes, eight days without water results in a 10.3% increase in plasma osmolality [unpublished data, S.M. Secor]. The increase in glucose concentrations observed in this study (by 52%) for the water snakes can largely be explained by the loss of plasma water and

resulting increase in solute concentrations. This mechanism is supported by the rapid drop in glucose concentration when water became available and snakes were able to drink. Drinking restored water to the plasma and therefore lowered solute concentrations. This was also observed in the other study; plasma osmolality was restored to normal hydrated levels within six hours of access to water. A second mechanism, not mutually exclusive of the first, is that the increase in blood glucose was generated from the stress of dehydration, as explained in the following.

Stress response

A universal response to stress is the release of glucocorticoids from the adrenal cortex gland that stimulates an increase in circulating metabolites, especially glucose. For snakes and other reptiles, the glucocorticoid steroid that is primarily secreted is corticosterone (shared with amphibians and birds). Corticosterone will induce an increase in gluconeogenesis resulting in an increase in circulating glucose. To entice a stress reaction of the water snakes, I manually turned snakes upside down and induced them to strike for 90 seconds. Within two hours, mean glucose levels had increased by 60% and continued to increase for the next ten hours before peaking following a 165% increase. Since snakes had neither eaten nor had been given any glucose, the increase must have been generated by rapid gluconeogenesis induced by the release of corticosterone. For red-sided garter snakes (*Thamnophis sirtalis*), males held in captivity within cloth bags for four hours experienced a 180% greater concentration of plasma glucose compared to control snakes [24]. A study that similarly evoked stress in five species of snakes observed more moderate levels of increase (11 - 16%) in blood glucose [10]. However, it was not identified for that study how long after the stress encounter the blood was drawn. For ectotherms, it may take a minimum of four hours before blood glucose significantly increases from stress.

Future studies

The aim of the presented study was to examine natural variation in the blood glucose concentrations of the diamondback water snake. This work served to establish the baseline range of resting values and to draw attention to the potential effects of hydration state and stress on blood glucose measurements. The next step of this project is to explore the capacity of the diamondback water snake, a strict carnivore, to regulate blood glucose levels when exposed to a glucose load. The questions to be addressed in future studies include: (1) Can snakes tolerate an increase in blood glucose resulting from glucose absorption? (2)

Can snakes rapidly lower blood glucose levels after they have risen from glucose absorption, and (3) is there a threshold of glucose absorption that exceeds their capacity to regulate?

References

- [1] Guyton AC & Hall JE. (1996) Textbook of Medical Physiology. WB Saunders Co., Philadelphia
- [2] Karasov WH & Diamond JM. (1988). Interplay between physiology and ecology in digestion. *BioScience*, 38:602-611.
- [3] Diamond JM. (1991). Evolutionary design of intestinal nutrient absorption: enough but not too much. *News Physiol. Sci.*, 6:92-96.
- [4] Caldwell MW, Nydam RL, Palci A & Apesteguia S. (2015). The oldest known snakes from the middle jurassic-lower cretaceous provide insights on snake evolution. *Nat. Commun*, 6:1-11.
- [5] Penhos JC. (1973) Studies on the endocrine pancreas of amphibians and reptiles. *Amer. Zool.*, 13:667-698.
- [6] Secor SM. (2008). Digestive physiology of the Burmese python, broad regulation of integrated performance. *J. Exp. Biol.*, 211:3767-3774.
- [7] Gibbons JW & Dorcas ME. (2004). North American Watersnakes: A Natural History. University of Oklahoma Press, Norman.
- [8] Cox CL & Secor SM. (2010). Integrated Postprandial Responses of the Diamondback Water Snake, *Nerodia rhombifer*. *Physiol. Biochem. Zool.*, 83:618-631.
- [9] Al-Badry KS & Nuzhy S. (1983). Hematological and biochemical parameters in active and hibernating sand vipers. *Comp. Biochem. Physiol.*, 74:137-141.
- [10] Britton SW & Kline RF. (1939). Emotional hyperglycemia and hyperthermia in tropical mammals and reptiles. *Am. J. Physiol.*, 125:730-734.
- [11] Houssay BA & Penhos JC. (1960). Pancreatic diabetes and hypophysectomy in the snake *Xenodon merremii*. *Acta Endocrinol.*, 35:313-323.
- [12] Martin JH & Bagby RM. (1973). Effects of fasting on the blood chemistry of the rattlesnake, *Crotalus atrox*. *Comp. Biochem. Physiol.*, 44A:813-820.
- [13] Otis VS. (1973). Hemocytological and serum chemistry parameters of the African puff adder, *Bitis arietans*. *Herpetologica*, 29:110-116.
- [14] Prado JL. (1946). Glucose tolerance test in Ophidia and the effect of feeding on their glycemia. *Rev. Can. Biol.*, 5:564-569.
- [15] Secor SM & Diamond JM. (1995). Adaptive responses to feeding in Burmese pythons: pay before pumping. *J. Exp. Biol.*, 198:1313-1325.
- [16] Skoczylas R & Sidorkiewicz E. (1974). Studies on the blood sugar level in the grass snake (*Natrix natrix L.*). *Comp. Biochem. Physiol.*, 48A:439-456.
- [17] Carmichael EB & Petcher PW. (1945). Constituents of the blood of the hibernating and normal rattlesnake, *Crotalus horridus*. *J. Biol. Chem.*, 161:693-696.
- [18] Secor SM, Fehsenfeld D, Diamond J & Adrian TE. (2001). Responses of python gastrointestinal regulatory peptides to feeding. *Proc. Natl. Acad. Sci.*, 98:13637-13642.
- [19] Cahill GF, Jr. (2006). Fuel metabolism in starvation. *Annu. Rev. Nutr.*, 26:1-22.
- [20] Champagne CD, Houser DS, & Crocker DE. (2006). Glucose metabolism during lactation in a fasting animal, the northern elephant seal. *Am. J. Physiol. Regul. Integr. Comp. Physiol.*, 291: R1129-1137.
- [21] Corssmit EP, Romijn JA, & Sauerwein HP. (2001). Regulation of glucose production with special attention to nonclassical regulatory mechanisms: a review. *Metabolism*, 50:742-755.
- [22] McCue MD. (2007). Western diamondback rattlesnakes demonstrate physiological and biochemical strategies for tolerating prolonged starvation. *Physiol. Biochem. Zool.*, 80:25-34.
- [23] Hervant F, Mathieu J, & Durand J. (2001). Behavioural, physiological and metabolic responses to long-term starvation and refeeding in a blind cave-dwelling (*Proteus anguinus*) and a surface-dwelling (*Euproctus asper*) salamander. *J. Exp. Biol.* 204:269-281.
- [24] Moore IT, Lemaster MP & Mason RT. (2000). Behavioural and hormonal responses to capture stress in the male red-sided garter snake, *Thamnophis sirtalis parietalis*. *Anim. Behav.*, 59:529-534.

Acknowledgments

I would like to extend my sincere appreciation to Dr. Stephen Secor for his guidance and resources throughout the entirety of this project. I would like to thank Gretchen Anderson, Matt Larkin, and Evan Menzel for their help in assisting me in blood drawings. I would also like to thank Gretchen Anderson, Ayla Jones, Shelly McCain and Evan Menzel for their comments in the preparation of this manuscript.

About the Author

Danny Laderberg is a senior from Norfolk, Virginia. He is a biology major and currently works in Dr. Stephen Secor's Laboratory of Evolutionary and Integrative Physiology. For over two years Danny's work has examined the capacity of the Diamondback water snake (*Nerodia rhombifer*) to regulate physiological performances with feeding and fasting. Danny's future plans are to work in veterinary medicine, possibly continuing his research in digestive physiology.

Microbial Effect on Age-Related Neurodegenerative Disorders

Anthony James

Faculty Mentor: Guy Caldwell – gcaldwel@ua.edu

Department of Biological Sciences, The University of Alabama, Tuscaloosa, Alabama 35487

*There is growing evidence that points attention toward more than coincidental correlation between the presence of certain bacteria—notably, *Chlamydia pneumoniae* and *Helicobacter pylori*—and viruses, such as enteroviruses and herpesviruses. These microbes can greatly affect important inflammatory pathways that are shared with pathways affected during the pathogenesis of age-related neurodegenerative disorders, such as Alzheimer's disease, Parkinson's disease, and amyotrophic lateral sclerosis. Furthermore, microbial agents, particularly viruses, can remain in latent forms while in the body and can cause damage to neurons depending upon the host's immune responses. More research regarding the potential interactions between genetics, environmental factors, and infectious agents is necessitated by a growing body of research that examines the consequences of the susceptibility of the aged immune system to a number of infectious agents. Findings from research into these potential interactions have the potential to alter the methods of diagnosis and treatment of age-related neurodegenerative disorders.*

Introduction

There is a growing base of evidence supporting an interaction between infectious agents and age-related neurodegenerative disorders, such as Alzheimer's disease and Parkinson's disease. The majority of this evidence has led to an increased understanding of the effects of infectious agents such as viruses, prion particles, and bacteria on the central nervous system and examines the effects of these infectious agents on the aged human immune system.

A notable case of the potential correlation between immune response, infectious agents, and age is seen in Alzheimer's disease. Although there is indeed a noted decrease in sufficient immune response in the aged immune system, there is also a paradoxical event in that a continuous proinflammatory status—a status that is a reflection of heightened immune response in aged immune systems—is now well documented as a factor in the development of age-related disorders not previously associated with immune reactivity, such as atherosclerosis (a hardening and narrowing of the arteries) and Alzheimer's disease [1]. Further evidence of this was shown in a study that demonstrated that Alzheimer's was less common in patients with rheumatoid arthritis who took anti-inflammatory medication due to their condition [1,2]. Contrastingly, continuous activation of innate system responses as well as proinflammatory responses have also been found to be associated with good health and have been noted in centenarians. It is yet unknown

whether the inflammatory processes that are noted in diseases such as Parkinson's and Huntington's are responses to neuronal degeneration or rather are pathogenic in nature. As will be further discussed, many infectious agents induce the same inflammatory response through the same or similar pathways as have been found to be linked to age-related neurodegenerative disorders. Many of these viral agents have been noted to remain in neurons for extensive periods of time, such as herpesvirus (simplex-1) [3]. Thus, it is also a possibility that agents that remain in the nervous system may trigger neurodegeneration as the individual ages. Additionally, there are key components of these disorders, such as protein aggregation and accumulation, that have been noted as having close association with infectious agents, particularly bacteria.

Role of aging in the pathogenesis and etiology of neurodegenerative diseases caused by microbial agents

In the elderly, there is a high incidence of severe infection that is coupled with a low efficacy of vaccination, which both present rather glaring problems in terms of an individual's ability to not only fight off infection but also to resist the development of infection as a primary defense. Due to the weakening of sufficient immune response to infectious agents as age increases, the central nervous system remains a primary point of extensive attack and damage for the elderly. This can be noted in such examples as West Nile Virus, which causes a disease with a rather low

fatality rate, in which those who are particularly susceptible to the life-threatening form of the disease are those who are elderly and/or immunocompromised [4]. There are many other pathogen-linked diseases for which the elderly are frequently cited as being among those who are most likely to succumb to the infection. Another notable example includes tuberculosis, caused by *Mycobacterium tuberculosis*, which has been studied as early as the 1940s [5] in regards to its fatality rate as a dependent variable of age. Furthermore, it has been posited that although the incidence of tuberculosis does not show an increase with age, the prevalence of the disease as well as poor outcomes, such as neurological sequelae, have been shown to have positive correlation with age [6,7].

Parkinson's Disease (PD)

Parkinson's disease (PD) is a progressive disorder of the nervous system that affects movement. In PD, certain neurons in the brain gradually break down or die. Many of the symptoms are due to loss of neurons that produce a chemical messenger in the brain called dopamine. When dopamine levels decrease, it causes abnormal brain activity, leading to signs of Parkinson's disease. Although the majority of PD cases diagnosed are without distinct etiology, there have been discovered genetic linkages to the disease via genes such as *DJ-1*, *PINK1*, and *PARKIN* [8,9]. Recent work on these genes punctuates the central importance of mitochondrial dysfunction, oxidative stress, and ATP depletion in the disease. There have also been a number of studies that have suggested that the risk for the development of PD may be increased in cases of certain dietary and environmental factors [10,11,12]. For example, there are data that show that dietary folate deficiency and elevated homocysteine levels endanger dopaminergic neurons [10] and that exposure, particularly subcutaneous exposure, to certain pesticides, such as rotenone, causes highly selective destruction of dopaminergic neurons as well as the aggregation of α -synuclein [11,12].

It has been shown that siblings of PD patients exhibited an increased probability of the presence of antibodies for the organism *Helicobacter pylori* than did control subjects [13]. Studies show that *H. pylori* can be a causative agent for ulcers [14] and that peptic ulceration is more common in PD patients when compared to controls [15]. Additionally, rats that have been infected with Japanese encephalitis (JE) virus have demonstrated parkinsonism-like symptoms caused by neuronal loss accompanied by gliosis [16]. Furthermore, it has been hypothesized that neuroviru-

lent influenza A virus and other viruses may be responsible for the formation of Lewy bodies and the subsequent death of nigral dopaminergic neurons in PD [17].

Amyotrophic Lateral Sclerosis (ALS)

Amyotrophic lateral sclerosis (ALS), also called Lou Gehrig's disease, is a neurological disease that attacks the neurons responsible for controlling voluntary muscles causing progressive paralysis and consequent death. Genetic mutations in genes encoding for Cu/Zn-superoxide dismutase are the cause of few cases of ALS [18]. Hypotheses surrounding the pathogenesis of the disease have led to the finding of abnormalities in lipid accumulation and metabolism as a point of concern. Research suggests that observed *in vivo* intensity enhancement in specific pathological regions of the brain, as seen by magnetic resonance imaging (MRI) in an ALS rat model, are correlated in part to lipid peroxidation and degeneration as well as the accumulation of lipids in the brainstem and mid-brain regions [19]. Additionally, accumulation of cholesteryl esters and ceramide has been shown to mediate oxidative stress and the induction of motor neuron death [20].

The RNA of enteroviruses has been found in the spinal fluid of ALS patients [21] and studies have suggested a possible association between herpesvirus and echovirus-7 seropositivity and the risk for the development of ALS [22]. Additionally, although mycoplasma infection has not been confirmed as a player in the pathogenesis of the disease, there has been a demonstrated link between mycoplasma infection and ALS [23]. Furthermore, there are ongoing studies examining the potential link between retroviral infections through the examination of HIV-positive patients who developed quickly progressing ALS-like symptoms and showed improvement while taking an antiretroviral therapy regimen [24].

Alzheimer's Disease (AD)

Alzheimer's disease (AD) is a neurodegenerative disease characterized by the accumulation of β -amyloid, neuronal death in areas of the brain involved in memory, and synaptic degeneration. The specific factors of pathogenesis and etiology of the disease are as of yet uncharacterized; however, inflammation is believed to have a significant role. The activation and perpetuation of pathways that may cause neurodegeneration are controlled by increased inflammatory molecules such as tumor necrosis factor- α (TNF- α) as

well as interleukin-6 (IL-6) and interleukin-1 β (IL-1 β) [25]. These findings may signify that those things that have the capability of altering these inflammatory molecules may also be able to alter the development and progression of AD. Additionally, β -amyloid can render neurons vulnerable to membrane peroxidation and the impairment of ion channels, which in turn can lead to apoptosis [26].

It has been reported that *C. pneumoniae* is present in the areas of neuropathology in the brains of AD patients [27,28], and it has most recently been suggested that investigating the distinct morphologies of *C. pneumoniae* in human blood samples from the geriatric population by electron microscopy, with other frontline diagnostic procedures, may clarify the diagnosis of mild cognitive impairment and late onset AD [29,30]. It is the summation of research of this kind that suggests that nervous system infection with *C. pneumoniae* should be considered a risk factor for sporadic AD.

It is known that infections in the elderly can result in cognitive impairment that demonstrates effects well beyond the scope of the infection itself; impairment in AD patients who experience a systemic infection can last several months post-resolution of the infection. Research also shows increased levels of IL-1 β before the development of cognitive impairment [31]. Furthermore, recent studies have also shown that AD patients infected by *H. pylori* tend to be more cognitively impaired [32] and also that positivity for anti-HSV IgM, a sign of reactivated infection, was found to almost double the risk for AD, whereas the presence of anti-HSV IgG antibodies did not affect the risk [33]. There have also been studies showing results such as that TNF- α and elevated numbers of antibodies against periodontal bacteria associate with AD and contribute to the AD diagnosis [34,35]. Results such as these encourage further research into potential interactions between infectious agents, genetics, and environment exerting influence upon the etiology of AD.

Conclusion

Well-documented neurodegenerative disorders such as Alzheimer's disease, amyotrophic lateral sclerosis (ALS), and Parkinson's disease are now undergoing further research that is continually punctuating potential linkages between microbial organisms and the etiology and pathogenesis of these diseases. The extensive effects that many of these infectious agents exert upon the shared inflammatory pathways

that have a significant role in neurodegenerative pathogenesis point toward a potential complex cause-effect relationship between the microbial world and the development of disease, especially when combined with genetic predispositions and environmental factors. Further exploration of these interactions will be particularly useful in understanding the possible etiologies of these neurodegenerative diseases as well as improving potential treatments, particularly in regard to predicted increases in the incidence of these diseases as the world sees a continually growing elderly population.

References

- [1] Akiyama H, Barger S, Barnum S, Bradt B, Bauer J, Cole GM, ... & Wyss-Coray T. (2000). Inflammation and Alzheimer's disease. *Neurobiology of aging*, 21(3), 383-421.
- [2] Grubeck-Loebenstien B, & Wick G. (2002). The aging of the immune system. *Advances in immunology*, 80, 243-284.
- [3] Mettenleiter TC. (2003). Pathogenesis of neurotropic herpesviruses: role of viral glycoproteins in neuroinvasion and transneuronal spread. *Virus research*, 92(2), 197-206.
- [4] Nedry M, & Mahon, CR. (2002). West Nile virus: an emerging virus in North America. *Clinical laboratory science: journal of the American Society for Medical Technology*, 16(1), 43-49.
- [5] Frost WH. (1940). The age selection of mortality from tuberculosis in successive decades. *The Milbank Memorial Fund Quarterly*, 61-66.
- [6] Stead WW, & Lofgren JP. (1983). Does the risk of tuberculosis increase in old age?. *The Journal of infectious diseases*, 951-955.
- [7] Kent SJ, Crowe SM, Yung A, Lucas CR, & Mijch AM. (1993). Tuberculous meningitis: a 30-year review. *Clinical infectious diseases*, 17(6), 987-994.
- [8] Dodson MW, & Guo M. (2007). Pink1, Parkin, DJ-1 and mitochondrial dysfunction in Parkinson's disease. *Current opinion in neurobiology*, 17(3), 331-337.
- [9] Moore DJ, Zhang L, Troncoso J, Lee MK, Hattori N, Mizuno Y, ... & Dawson VL. (2005). Association of DJ-1 and parkin mediated by pathogenic DJ-1 mutations and oxidative stress. *Human molecular genetics*, 14(1), 71-84.
- [10] Duan W, Ladenheim B, Cutler RG, Kruman II, Cadet JL, & Mattson MP. (2002). Dietary folate deficiency and elevated homocysteine levels endanger dopaminergic neurons in models of Parkinson's disease. *Journal of neurochemistry*, 80(1), 101-110.
- [11] Alam M, & Schmidt WJ. (2002). Rotenone destroys dopaminergic neurons and induces parkinsonian symptoms in rats. *Behavioural brain research*, 136(1), 317-324.
- [12] Sherer TB, Kim JH, Betarbet R, & Greenamyre JT. (2003). Subcutaneous rotenone exposure causes highly selective dopaminergic degeneration and α -synuclein aggregation. *Experimental neurology*, 179(1), 9-16.
- [13] Charlett A, Dobbs RJ, Dobbs SM, Weller C, Brady P, & Peterson DW. (1999). Parkinsonism: siblings share Helicobacter pylori seropositivity and facets of syndrome. *Acta neurologica scandinavica*, 99(1), 26-35.
- [14] Suerbaum S, & Michetti P. (2002). Helicobacter pylori infection. *New England Journal of Medicine*, 347(15), 1175-1186.
- [15] Szabo S. (1979). Dopamine disorder in duodenal ulceration. *The Lancet*, 314(8148), 880-882.
- [16] Ogata A, Tashiro K, Nukuzuma S, Nagashima K, & Hall WW. (1997). A rat model of Parkinson's disease induced by Japanese encephalitis virus. *Journal of neurovirology*, 3(2), 141-147.
- [17] Takahashi M, & Yamada T. (1999). Viral etiology for Parkinson's disease--a possible role of influenza A virus infection. *Japanese journal of infectious diseases*, 52(3), 89-98.
- [18] Franco MC, Dennys CN, Rossi FH, & Estévez AG. (2013). Superoxide Dismutase and Oxidative Stress in Amyotrophic Lateral Sclerosis.
- [19] Machtoub L, Bataveljic D, & Andjus PR. (2011). Molecular imaging of brain lipid environment of lymphocytes in amyotrophic lateral sclerosis using magnetic resonance imaging and SECARS microscopy. *Physiol. Res*, 60(1), S121-S127.
- [20] Cutler RG, Pedersen WA, Camandola S, Rothstein JD, & Mattson MP. (2002). Evidence that accumulation of ceramides and cholesterol esters mediates oxidative stress-induced death of motor neurons in amyotrophic lateral sclerosis. *Annals of neurology*, 52(4), 448-457.
- [21] Majoor-Krakauer D, Willems PJ, & Hofman A. (2003). Genetic epidemiology of amyotrophic lateral sclerosis. *Clinical genetics*, 63(2), 83-101.
- [22] Cermelli C, Vinceti M, Beretti F, Pietrini V, Nacci G, Pietrosemoli P, ... & Portolani M. (2003). Risk of sporadic amyotrophic lateral sclerosis associated with seropositivity for herpesviruses and echovi-

rus-7. *European journal of epidemiology*, 18(2), 123-127.

[23] Nicolson GL, Nasralla MY, Haier J, & Pomfret J. (2002). High frequency of systemic mycoplasmal infections in Gulf War veterans and civilians with Amyotrophic Lateral Sclerosis (ALS). *Journal of clinical neuroscience*, 9(5), 525-529.

[24] Anand KS, Wadhwa A, Garg J, & Mahajan RK. (2014). Amyotrophic Lateral Sclerosis-Like Presentation in a HIV-Positive Patient. *Journal of the International Association of Providers of AIDS Care (JIAPAC)*, 2325957414535254.

[25] Akiyama H, Arai T, Kondo H, Tanno E, Haga C, & Ikeda K. (2000). Cell mediators of inflammation in the Alzheimer disease brain. *Alzheimer Disease & Associated Disorders*, 14(1), S47-S53.

[26] Hensley K, Carney JM, Mattson MP, Aksenova M, Harris M, Wu JF, ... & Butterfield DA. (1994). A model for beta-amyloid aggregation and neurotoxicity based on free radical generation by the peptide: relevance to Alzheimer disease. *Proceedings of the National Academy of Sciences*, 91(8), 3270-3274.

[27] Gérard, H. C., Dreses-Werringloer, U., Wildt, K. S., Deka, S., Oszust, C., Balin, B. J., ... & Hudson, A. P. (2006). Chlamydia (Chlamydia) pneumoniae in the Alzheimer's brain. *FEMS Immunology & Medical Microbiology*, 48(3), 355-366.

[28] Hammond, C. J., Hallock, L. R., Howanski, R. J., Appelt, D. M., Little, C. S., & Balin, B. J. (2010). Immunohistological detection of Chlamydia pneumoniae in the Alzheimer's disease brain. *BMC neuroscience*, 11(1), 121.

[29] Brandt J, Cader A, Semler L, Hammond C, Bell M, Devins M, ... & Appelt D. (2014). Electron microscopy studies elucidate morphological forms of Chlamydia pneumoniae in blood samples from patients diagnosed with mild cognitive impairment (MCI) and Alzheimer's disease (AD)(LB81). *The FASEB Journal*, 28(1 Supplement), LB81.

[30] Balin BJ, & Appelt DM. (2001). Role of infection in Alzheimer's disease. *JAOA: Journal of the American Osteopathic Association*, 101(12 suppl 1), 1S-6S.

[31] Holmes C, El-Okl M, Williams AL, Cunningham C, Wilcockson D, & Perry VH. (2003). Systemic in-

fection, interleukin 1 β , and cognitive decline in Alzheimer's disease. *Journal of Neurology, Neurosurgery & Psychiatry*, 74(6), 788-789.

[32] Roubaud-Baudron C, Krolak-Salmon P, Quadrio I, Mégraud F, & Salles N. (2012). Impact of chronic *Helicobacter pylori* infection on Alzheimer's disease: preliminary results. *Neurobiology of aging*, 33(5), 1009-e11.

[33] Lövhelm H, Gilthorpe J, Adolfsson R, Nilsson LG, & Elgh F. (2014). Reactivated herpes simplex infection increases the risk of Alzheimer's disease. *Alzheimer's & Dementia*.

[34] Stein PS, Steffen MJ, Smith C, Jicha G, Ebersole JL, Abner E, & Dawson III D. (2012). Serum antibodies to periodontal pathogens are a risk factor for Alzheimer's disease. *Alzheimer's & Dementia*, 8(3), 196-203.

[35] Kamer AR, Craig RG, Pirraglia E, Dasanayake AP, Norman RG, Boylan RJ, ... & de Leon MJ. (2009). TNF- α and antibodies to periodontal bacteria discriminate between Alzheimer's disease patients and normal subjects. *Journal of neuroimmunology*, 216(1), 92-97.

About the Author

Anthony "A.J." James is a rising senior at The University of Alabama who hails from Columbus, GA. He is double majoring in microbiology and Spanish. A.J.'s scientific interests revolve around investigating microbial linkages to diseases that have personally affected family and friends, such as Alzheimer's, HIV/AIDS, and Parkinson's.

JOSHUA was made possible by the
following organizations:

University of Alabama
Office of the President

Tri-Beta National Honor Society
Kappa Beta Chapter

Howard Hughes Medical Institute

National Science Foundation

Computer Based Honors Program

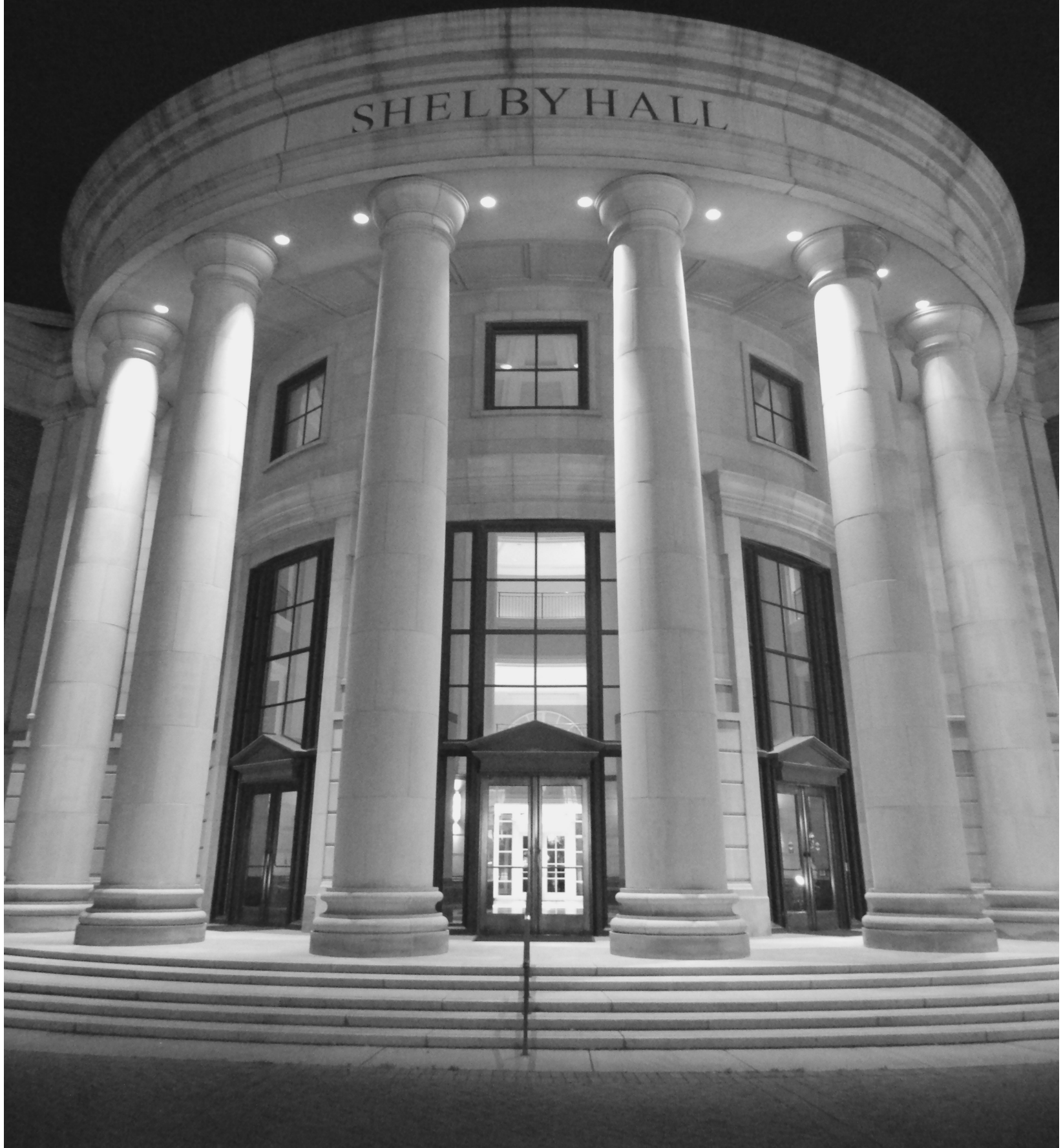
And by the 2014-2015 JOSHUA Editing Staff

2016 Submission Guidelines

We accept articles from current undergraduate students at The University of Alabama (UA). If you are a graduate student or recent alumnus of UA, we will consider your article if the majority of your work was conducted while you were an undergraduate at UA. Undergraduate students from other institutions may submit; however, priority will be given to those who conducted their research at UA.

1. Your name, e-mail address, and phone number must be included.
2. Your submission must relate to science or health.
3. Your work must be sponsored by a faculty member.
4. The length of your submission must be between 2000 and 4500 words. We will accept longer submissions if the author can limit the submission to the required length for the publication, and any extra material is able to be published online.
5. Figures, charts, and graphs are allowed but not required. (Note: The color will be mostly black and white.)
6. Your paper must contain an abstract.
7. Your citations must follow the guidelines listed on our website at BAMA.UA.EDU/~JOSHUA.
8. The deadline for submission is February 12, 2016.
9. E-mail submissions to joshua.alabama@gmail.com

SHELBY HALL



THE UNIVERSITY OF ALABAMA®